J. Phys. Chem. A **2008,** *112,* 10453–10468

Unraveling Complex Three-Body Photodissociation Dynamics of Dimethyl Sulfoxide: A Femtosecond Time-Resolved Spectroscopic Study

Jr-Wei Ho, Wei-Kan Chen,[†] and Po-Yuan Cheng*

Department of Chemistry, National Tsing Hua University, Hsinchu, Taiwan, R. O. C.

Received: June 2, 2008; Revised Manuscript Received: July 18, 2008

Photodissociation of dimethyl sulfoxide at 200 nm has been studied using femtosecond time-resolved spectroscopy. The temporal evolutions of the initial state, intermediates, and products (CH_3 and SO) were measured by means of fs pump−probe mass-selected multiphoton ionization and laser-induced fluorescence. Femtosecond time-resolved photofragment translational spectroscopy was also employed to measure the CH_3 product kinetic energy distributions as a function of reaction time. The ionization experiments revealed that there are at least three major CH_3 product components, whereas the fluorescence experiments indicated that two SO product components are present. The combination of experimental and theoretical results suggested a complex multichannel mechanism involving both concerted and stepwise three-body dissociation pathways.

1. Introduction

Molecular many-body dissociation remains as an intriguing and yet challenging problem in the field of reaction dynamics.[1,2] The main issues are to understand the temporal sequence of multiple bond breaking, energy partitioning among various degrees of freedom, and product-state correlation. Important insights into the many-body dissociation dynamics have been attained from studies using conventional photofragment translational spectroscopy (PTS).[1−8] Recent developments in coincidence spectroscopy have achieved kinematically complete measurements for three-body dissociation by detecting all fragments in coincidence.[9] However, such a technique constitutes a substantial experimental challenge and is most suitable for dissociative photodetachment and dissociative photoionization processes.[9,10] Femtosecond (fs) real-time spectroscopy,[11,12] which measures the temporal evolution of the initial state, intermediate, and products, provides an alternative mean to elucidate the many-body dissociation mechanism.[13,14] A variety of detection schemes can be employed to achieve state and mass selection with fs time resolution.[14] If all fragments are detected, products arising from the same elementary step can be identified based on their temporal correlation.

In the case of three-body dissociation in which an energized molecule breaks up into three fragments, the two extreme descriptions of the mechanism, namely, *concerted* versus *stepwise*, have been the main focus of many previous studies.[1−8,15−18]As pointed out elsewhere,[16,19] the true concertedness must address the nuclear motion in reference to the time scales of the reaction coordinate. Numerous molecular systems have been investigated to elucidate the three-body photodissociation dynamics;[1,2] among them, acetone is probably the most well-studied system.[15,17,19−25] Being the simplest aliphatic ketone, acetone possesses two equivalent α-C−C bonds that can break at sufficiently high energy to produce three fragments. Dimethyl sulfoxide (DMSO) is another interesting system that bears many similar aspects to acetone and thus has also drawn extensive attention.[26−32] UV absorption of DMSO starts at about 240 nm and extends into the deep UV region, with generally broad and continuous spectral features exhibiting no or overlapping vibronic structures.[33] As shown in Figure 1, photoexcitation of DMSO in the UV region is energetically feasible to break the two equivalent C−S bonds to produce $CH_3 + SO + CH_3$, that is, a three-body dissociation. Although DMSO is usually considered as the sulfur analogue of acetone, it possesses very different bonding characteristics due to the presence of the sulfur atom. The C−S bond enthalpies are 214 and 220 kJ/mol in DMSO and CH_3SO,[34,35] respectively, while the corresponding C−C bond enthalpies in acetone and CH_3CO are 350 and 33 kJ/mol,[15,36] respectively. The very different bond energy partition results in a significant effect on the dissociation dynamics in these two molecules.

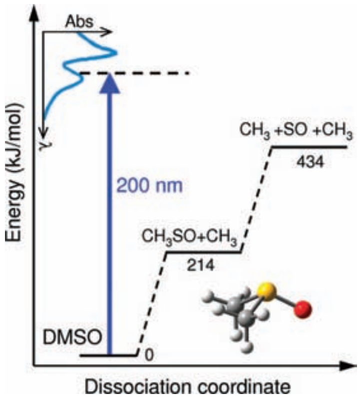

Figure 1. Schematic energy level diagram for photodissociation of DMSO along the two C−S bonds. The trace in the upper-left corner is a vapor-phase absorption spectrum of DMSO taken from ref 33. Also shown is the optimized DMSO ground-state structure as described in the text.

Chen et al.[26] studied the product-state distributions resulting from DMSO photodissociation at 193 nm using laser-induced fluorescence (LIF) for SO and resonance-enhanced multiphoton ionization (REMPI) for CH_3. They observed an inverted SO product vibrational energy distribution peaking at $v'' = 2$ and a near unity SO quantum yield. Combining this with the low rotational temperature of SO and the lack of evidence of two

---

* To whom correspondence should be addressed. E-mail: pycheng@mx.nthu.edu.tw.

[†] Current address: National Synchrotron Radiation Research Center, Hsinchu, Taiwan, R. O. C.

10.1021/jp804847y CCC: $40.75

CH_3 distributions, they proposed that the photodissociation of DMSO at 193 nm proceeds via a concerted three-body dissociation mechanism.[26]

Zhao et al.[29] studied photodissociation of DMSO at 193 nm using photofragment translational spectroscopy (PTS). They observed and identified the reaction intermediate, CH_3SO, as a stable primary product. The analysis of the TOF data provided evidence that the majority of SO is formed via a stepwise mechanism. Their analyses also indicated that ~53% of the CH_3SO intermediate undergoes a secondary dissociation to produce $CH_3 + SO$, giving a quantum yield of ~1.53 for CH_3. They also reported that the product channel $CH_3SCH_3 + O$ was not observed within the sensitivity of their experiment.[29]

Blank et al.[27] also studied the photodissociation of DMSO-d_6 and -h_6 at 193 nm using PTS with tunable vacuum UV product detection. They, too, observed the CH_3SO intermediate and concluded that the reaction mainly proceeds via a stepwise mechanism involving multiple reaction channels. Two competing primary dissociation channels were suggested to account for the observed translational energy distributions, a major primary dissociation channel (83% in DMSO-d_6 and 73% in DMSO-h_6) that occurs on the ground electronic state following internal conversion and a competing channel that occurs on an excited electronic surface leading to the methyl radical and the electronically excited CH_3SO. A fraction of the hot CH_3SO (CD_3SO) intermediates produced in the ground-state channel undergoes a secondary dissociation to yield CH_3 (CD_3) and SO. The quantum yields for CH_3 (CD_3) and SO were determined to be 1.4 ± 0.1 and 0.6 ± 0.1, respectively.[27] A minor (<5%) hydrogen atom elimination channel was reported for the secondary decomposition of CH_3SO and was thought to involve tunneling because of the negative detection of analogous secondary C−D bond cleavage in the case of DMSO-d_6.[27]

Rudolph et al.[28] studied the 193 and 222 nm photodissociation of DMSO-d_6 using infrared diode laser absorption spectroscopy to measure the CD_3 products. The results were consistent with a stepwise mechanism, and the CD_3 quantum yield was determined to be 1.4 at 193 nm and 1.2 at 222 nm. The fraction of the CD_3 vibrational ground state was found to account for about 30% of the total methyl products produced in the reaction for both photolysis wavelengths.[28] Thorson et al.[30] investigated the photodissociation of DMSO at 210 and 222 nm using VUV laser ionization for product detection in a time-of-flight mass spectrometer (TOF-MS). The CH_3 quantum yield was determined to be 1.1 ± 0.1 in the 222 nm photolysis and 1.3 ± 0.1 in the 210 nm photolysis. They also measured the SO internal energy distribution by means of laser-induced fluorescence (LIF) spectroscopy. Analyses indicated that the vibrational energy distribution of the SO products peaks at $v'' = 1$ for both photolysis wavelengths.[30] More recently, Pino et al.[31] studied the photodissociation of DMSO-d_6 at four different wavelengths in the 204−227 nm region using REMPI and TOF-MS to measure the kinetic energy distributions and internal energies of CD_3 products. They observed a fast anisotropic CD_3 channel ($\beta \sim 0.3$),[31,32] and the results are consistent with the three dissociation channels proposed by Blank et al.[27]

Unlike the more well studied case of acetone, photodissociation of DMSO has not been subjected to ultrafast time-resolved study. Here, we present results of our recent investigation on the photodissociation dynamics of DMSO at 200 nm using fs pump−probe spectroscopy. The temporal evolutions of the initial state, intermediates, and all products (CH_3 and SO) were measured by means of fs pump−probe mass-selected multiphoton ionization (MPI) and LIF. Femtosecond time-resolved photofragment translational spectroscopy[24,37] was also used to measure the CH_3 product translational energy distributions as a function of reaction time. Electronic structure calculations were carried out to provide theoretical support. The combination of experimental and theoretical results led us to conclude that the reaction proceeds through a complex multichannel mechanism involving both concerted and stepwise pathways.

2. Experimental Section

Three types of experiments were carried out in this study. In all experiments, the laser pulses were derived from a fs laser system consisting of a self-mode-locked Ti:sapphire laser (Spectra Physics, Tsunami), a 1 kHz chirped-pulse regenerative amplifier (CPA; Spectra Physics, Spitfire), and a five-pass optical parametric generator/amplifier (OPA; Light Conversion, TOPAS). The oscillator wavelength was tuned to around 800 nm, and the output pulses were selectively amplified in the CPA, producing fs pulses of ~1 mJ/pulse in energy and ~120 fs fwhm in duration at a repetition rate of 1 kHz. The CPA output was split into two parts by a beam splitter. The weaker split portion (~30%) was first directed through a retroreflector mounted on a computer-controlled translation stage and was then sent into a harmonic generator to produce the fourth harmonic at ~200 nm by mixing the CPA output fundamental at 800 nm with the third harmonic at 266 nm in a 0.1 mm thick BBO crystal. These fs pulses at 200 nm were used as the pump to excite DMSO in all three types of experiments described below.

2.1. Femtosecond Pump−REMPI−Probe Experiments. In this type of experiment, DMSO was excited in a supersonic molecular beam with fs pump pulses at 200 nm to initiate the reaction. The temporal evolution of the initial state, intermediate, and CH_3 product was measured by the delayed probe pulses via mass-selected MPI in a TOF-MS. The major split portion (~70%) of the CPA output was used to pump the OPA, whose signal output at ~1334 nm was subsequently frequency-doubled twice in two thin BBO crystals to produce probe pulses at ~333.5 nm for the 2 + 1 resonance-enhanced multiphoton ionization (REMPI) detection of CH_3 radicals.[38] With the ~2 nm bandwidth, the probe laser covers the entire rotational contour of the $3p^2A_2'' \leftarrow 2p^2A_2''0_0^0$ transition of nascent CH_3 products.[30,31] The same 333.5 nm pulses were also used to probe the initial state and CH_3SO intermediate. Other probe wavelengths at 329.5 and 350 nm were also produced in similar manners.

The pump (200 nm) and probe beams were collinearly recombined via a dichroic mirror and focused through a $f = 50$ cm lens into the extraction region of a homemade two-stage TOF-MS housed in a conventional two-chamber differentially pumped molecular beam apparatus. A 40 mm diameter microchannel plate (MCP; Burle TOF-4000) assembly located at the end of the 55 cm flight tube was used as the ion detector. A DMSO/He/Xe gas mixture prepared by flowing 1% Xe in He gas (~700 torr) over room-temperature liquid DMSO was expanded through a 100 μm diameter pinhole to produce a continuous supersonic jet in the first chamber. The nozzle was heated to ~100 °C to avoid cluster formation. The jet was skimmed before entering the second chamber, where it was intersected by the fs laser pulses in the extraction region of the TOF-MS. The molecular beam, laser, and TOF-MS axes are all perpendicular to each other.

A MgF_2 half-wave plate and a Berek compensator were used to control the polarization orientations of the pump and probe, respectively, before they entered the molecular beam apparatus.

For all transients presented here, the angle between the pump- and probe-laser polarizations was set at the magic angle (54.7°) to minimize the rotational coherence effect. Pulse energies were kept low (~0.2−0.5 μJ/pulse) for the pump laser to ensure one-photon excitation, while slightly higher pulse energies were used for the probe (~0.5−2.0 μJ/pulse) to facilitate MPI. The cross correlation of the pump and probe pulses was ~230 fs fwhm as determined in situ by the nonresonant pump−probe MPI transient of Xe atom. Femtosecond mass-selected transients were obtained by monitoring the ion intensities of specific mass channels with a boxcar integrator (Stanford Research SR250) while the pump versus probe delay time was scanned. Transients were recorded for the parent, CH_3SO intermediate, and CH_3 product at *m/e* 78 ($CH_3SOCH_3^+$), 63 (CH_3SO^+), and 15 (CH_3^+), respectively.

2.2. Femtosecond Time-Resolved Photofragment Translational Spectroscopy. In the second type of experiment, we combined the fs pump−REMPI−probe detection and the kinetic-energy-resolved TOF-MS (KETOF) to measure the kinetic energy distribution of the CH_3 products at different reaction times. Detailed description of our fs-KETOF experiment and data analyses procedures have been given elsewhere.[24,37] The experimental setups are nearly the same as those described above except that the TOF-MS was operated with a much lower extraction field of about 100 V/cm to disperse the kinetic energy. Unless otherwise indicated, the pump- and probe-laser polarizations were oriented at 54.7° with respect to the TOF-MS axis on opposite sides.

Two modes of experiments were carried out. In the "snapshot" mode, the translation stage was fixed at a specific pump−probe delay time, and the corresponding KETOF spectrum, that is, the ion arrival time distribution, of CH_3 ions was recorded. A digital storage oscilloscope (LeCroy LT372, 500 MHz) was used to record the spectra with a sampling rate of 4 Gs/s (0.25 ns/pt). Data acquisition was automated by using a computer program which stops the translation stage at several preselected positions and records the KETOF spectra by averaging the ion TOF distributions for a certain number of laser shots. Background spectra due to one-laser ionization of the pump and probe alone were prerecorded by blocking one laser at a time with computer-controlled shutters at the beginning of each scan and were subtracted from the subsequently recorded pump + probe spectra. To avoid long-term signal drift, the program scans through these preselected positions repetitively until satisfactory spectra are accumulated. The final KETOF spectra were obtained by averaging all spectra taken at the same delay times.

The KETOF spectra were first transformed into v_z distributions using a calibration factor. Because the molecular beam is orthogonal to the TOF-MS axis, the laboratory v_z thus obtained is equivalent to $v_{z,\mathrm{COM}}$, or v_z with respect to the center-of-mass (COM) of the reaction precursor. The raw data were then smoothed to remove high-frequency noise before they were transformed into speed distributions according to procedures described elsewhere.[24,37] Only the first-half (positive v_z) portion of each spectra was used for analyses. The overall speed resolution under the present conditions was about 400 m/sec (at ~3500 m/sec) for $m/e = 15$, as estimated from the measured CH_3 speed distributions for CH_3I photodissociation at 266 nm.

2.3. Femtosecond Pump−LIF−Probe Experiment. The fs-LIF experiment for the SO product probing was carried out in a gas flow cell. DMSO vapor was slowly introduced into the cell through a needle valve, and the cell was continuously pumped by an oil-free scroll pump to maintain a pressure of ~120 mTorr. DMSO vapor in the cell was excited by fs pump pulses at 200 nm, and the temporal evolution of the free $SO(X^3\Sigma^-)$ product formation was measured by monitoring the SO B ← X LIF signal with delayed fs probe pulses. Different $SO(X^3\Sigma^-)$ vibrational levels ($v'' = 1, 2, 3$) can be selectively monitored by tuning the probe laser to the corresponding transitions.[39−41] In order to minimize the possibility of overlapped detection, we chose the following (v',v'') vibronic bands for different v'' probing: (2,1) for $v'' = 1$ probing at 241.5 nm, (2,2) for $v'' = 2$ probing at 248.2 nm, and (1,3) for $v'' = 3$ probing at 260.1 nm. The signal output of the OPA was mixed with the residual 800 nm pump pulse to obtain fs pulses between 480 and 520 nm, which were subsequently doubled to produce the probe pulses at the desired wavelengths. The probe pulses thus produced have spectral bandwidths of ~1.0 nm covering the major portion of each selected nascent SO B ← X vibronic bands.[26,30]

The pump and probe beams were collinearly recombined via a dichroic mirror and focused through a $f = 50$ cm lens into the gas cell. The fluorescence was collected at a right angle and detected by a photomultiplier tube (Hamamatsu R928). A band-pass filter centered at 330 nm and two long-pass filters (290 nm cutoff) were placed in the light collection system to reduce the scattered light and to ensure that only fluorescence photons in the 300−370 nm[40] spectral region could be efficiently detected. The signal from the photomultiplier tube was sent to a digital oscilloscope and a boxcar gate integrator for signal averaging. The fs transients were obtained by monitoring the fluorescence signal as a function of the pump−probe delay time. Alternatively, the translation stage could be stopped at a certain delay time while the transient fluorescence signal was recorded by the digital oscilloscope.

3. Results and Data Analyses

3.1. The Parent (DMSO) and Intermediate (CH_3SO) Transients. Figure 2 shows typical DMSO and CH_3SO transients obtained by monitoring the corresponding ion intensity as a function of pump−probe delay time (*t*). Also shown in Figure 2 is a Xe atom transient, which resembles the instrument response function (IRF), recorded in situ under the same experimental condition. The parent ion signal (Figure 2A) decays very rapidly after the initial instantaneous rise and can be fit to an exponential decay of 30 ± 10 fs convoluted with a Gaussian IRF of 230 fs (fwhm). The fs pump laser excites DMSO to an excited state in the spectral region at around 200 nm. The initially excited state is then ionized by absorbing at least one probe photon at 333.5 nm, reaching a total energy of ~9.92 eV that is above the DMSO adiabatic ionization potential (IP) of 9.1 eV.[33] Thus, the parent transient observed here immediately indicates that the initially excited state at 200 nm is extremely short-lived. The CH_3SO transient (Figure 2B) also exhibits a nearly instantaneous rise followed by a rapid decay, indicating that either the ground or excited state of the CH_3SO intermediate lives for a very short time (<0.1 ps). A very small long-time component is also present in the CH_3SO transient and is more prominent when the probe wavelength is tuned to 267 nm, suggesting that a fraction of the intermediate is long-lived. The fitting shown in Figure 2B includes an initial-state dissociative ionization (DI) and other components that will be explained below. DI of the initial state can occur in this case because ionization of neutral CH_3SO requires at least two probe photons at 333 nm, and thus, two-photon absorption of the DMSO initial state is inevitable when slightly stronger probe pulses are used for recording CH_3SO transients. This produces highly energetic parent ions that can decompose into the CH_3SO and/or CH_3

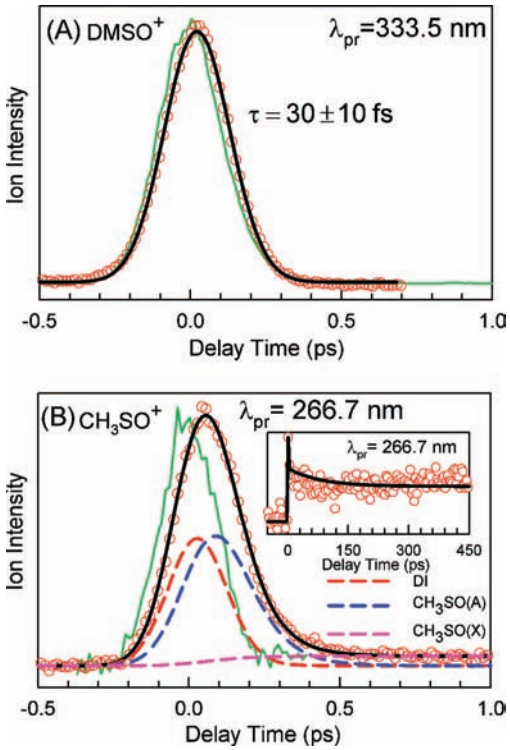

Figure 2. Transients obtained by monitoring (A) the DMSO ion (*m*/*e* 78) and (B) the CH_3SO ion (*m*/*e* 63) signal as a function of pump−probe delay time. Open circles are the experimental data, and the black solid lines are the best fit to the model described in the text. The green traces are Xe atom transients recorded in situ under the same experimental conditions and resemble the cross correlation of the pump and probe pulses. The dashed lines in (B) are the decomposed components included in the fit. The inset in (B) shows a long-time-scale CH_3SO transient. Owing to the much larger step size used, the large signal near zero delay time is not faithfully represented, and thus, the small long-time component appears to be more prominent.

ions. Consequently, the temporal behavior of the DI component should resemble that of the initial-state dynamics. Similar DI processes also occur in neutral CH_3 product probing in which three 333 nm photons are required and may come from both the parent and intermediate species.

3.2. The CH_3 Transients. Figure 3A shows typical CH_3 transients measured at three probe wavelengths. The 333.5 nm transient (trace a), probed via the CH_3 $3p^2A_2'' \leftarrow 2p^2A_2''0_0^0$ 2 + 1 REMPI transitions,[38] exhibits a rapid initial rise followed by a much slower one that reaches a plateau at ~450 ps. The signal then stays constant up to the longest delay (~1.8 ns) available in this study. The general rising behavior is consistent with the REMPI detection employed here and is expected to reveal the temporal evolution of the CH_3 products. The slower component can be described by an exponential rise of 90 ± 10 ps and makes up about 35% of the total signal. The much faster rise is more complex, as revealed in the early time transients displayed in Figure 3B. Except for a sharp temporal feature near the zero delay time, other transient components exhibit a pump-laser-irradiance dependence consistent with one-photon excitation, as shown in Figure 4. Although this sharp feature diminishes more rapidly as the pump-laser irradiance decreases, it is still present and mixed in with other components even at the lowest pump-laser pulse energy (0.2 μJ/pulse) used here. This temporal feature is very similar in shape to the CH_3 transient probed at 350 nm (Figure 3B trace c), which is completely off any known CH_3 REMPI transitions in this spectral region. Because the off-resonance transient was found to be rather insensitive to the variation of probe wavelength at around 350 nm, we concluded that the same off-resonance contribution is also present in the resonance-enhanced 333.5 nm transient and must be included in the fitting model described below. The resemblance of this off-resonance component to the parent and intermediate transients suggests that it is probably due to DI of the initial state and/or intermediate species that decompose into the methyl ion mass channel.

In addition to the DI contribution near time zero, the early time CH_3 transient also contains other temporal components. Combined inspections of the transients and time-resolved CH_3 speed distributions described below suggested that there are at least two neutral CH_3 components in the early time (<1 ps), a rapidly rising component associated with high-speed CH_3 fragments and a slower rising component associated with lower-speed CH_3 fragments. The temporal behavior of the high-speed component can be isolated by gating the outer region of the CH_3 KETOF profile, as shown in the Figure 3B inset and trace b. This high-velocity-selected transient indicates that the high-speed component does rise rapidly and is better described as an exponential rise of 50 ± 30 fs with a coherent delay of 130 ± 30 fs. The existence of a second rise component with a time constant on the order of a few hundred fs is evident from the slower rising behavior in the early time transient (Figure 3B trace a) between 0.2 and 0.8 ps. Using a kinetic model[42] derived from the proposed mechanism discussed below, we obtained a satisfactory fit to the early time transient, as shown in Figure 3B (trace a), and the time constant of the slower rise component was found to be 350 ± 50 fs. It should be emphasized here that the existence of two neutral CH_3 components within 1.0 ps and their order-of-magnitude rise times are self-evident in the data and are perceptible prior to the kinetic modeling, which was only meant to test the validity of the proposed mechanism and to obtain a more quantitative description of the reaction.

We also probed the umbrella-mode excited CH_3 ($v_2'' = 1$) via the $3p^2A_2'' \leftarrow 2p^2A_2''2_1^1$ hot-band transition at 329.5 nm (Figure 3A trace b) and found similar temporal behaviors to those observed for vibrationless CH_3. The rise time of the slowest component slightly increased to 110 ± 10 ps.

3.3. Time-Resolved CH_3 KETOF Spectra. Figure 5 shows the fs time-resolved CH_3 KETOF spectra obtained at several pump−probe delay times. Before 1 ps (Figure 5A), the KETOF profiles rapidly become broader with increasing delay time, indicating that a high-speed component emerges in this time scale. From 1 to 450 ps (Figure 5B), the amplitudes of the KETOF spectra slowly increase, but the widths become narrower. This indicates that a low-speed component slowly appears in this time range. Beyond 450 ps, the KETOF profile stays constant with time, consistent with the CH_3 transients shown in Figure 3A. The laser pulse energies used to obtain these KETOF spectra were similar to those used for recording the transients shown in Figure 3. Lowering the laser pulse energy by a factor of 2 did not change the shape of the KETOF spectra, indicating that the space-charge effect was not significant in the present case.

Figure 5C shows two KETOF spectra measured at $t = 1$ ps with the pump laser being polarized parallel and perpendicular to the TOF-MS (z) axis. The slightly broader parallel-polarization distribution clearly indicates a positive recoil anisotropy parameter (β). An apparent anisotropy function can be evaluated as a function of v_z according to $\tilde{\beta}(v_z) = 2[I_\parallel(v_z) - I_\perp(v_z)]/[I_\parallel(v_z) + 2I_\perp(v_z)]$,[32,43] and the result is displayed in the Figure 5C inset. Because the v_z distribution is the projection of the recoil velocity distribution onto the z axis, $\tilde{\beta}(v_z)$ does not represent the true

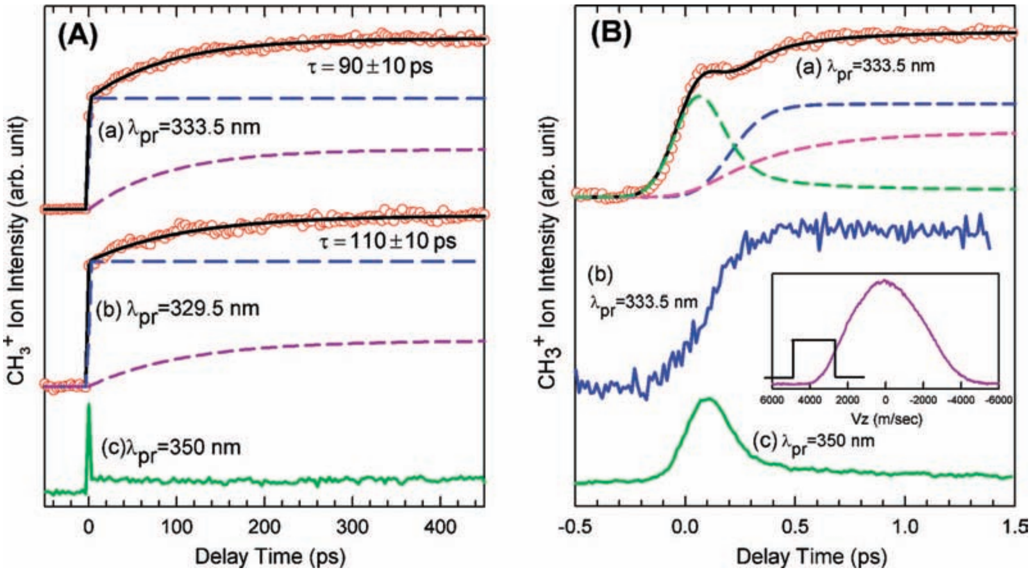

Figure 3. (A) Typical transients obtained by monitoring CH_3 ion (*m/e* 15) signal with λ_{pr} = (a) 333.5, (b) 329.5, and (c) 350 nm. Other experimental conditions are nearly identical for all three transients. (B) Short-time-scale transients taken with λ_{pr} = (a, b) 333.5 and (c) 350 nm. Trace (b) in (B) was recorded under the velocity-gating mode with the gate position shown in the inset. The black lines are the best fit of data to the model described in the text, and the dashed lines are the decomposed components.

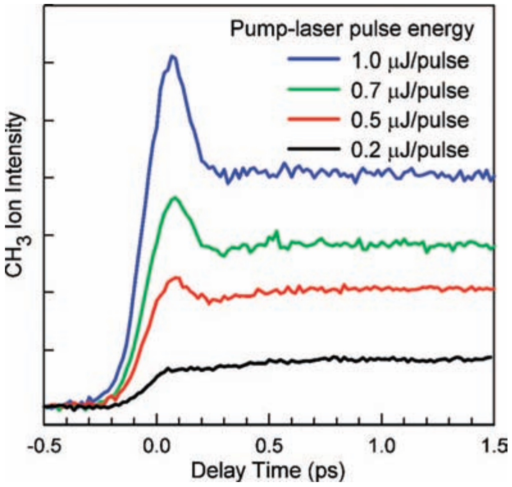

Figure 4. Pump-laser-irradiance dependence of the short-time-scale CH_3 transient measured with a constant probe-laser (333.5 nm) pulse energy. From top to bottom, the pump-laser pulse energies are 1.0, 0.7, 0.5, and 0.2 μJ/pulse.

anisotropy parameter function $\beta(v)$. Only in the highest v_z region, where $v_z \cong v$, is the value of $\tilde{\beta}(v_z)$ a good approximation to the actual value of $\beta(v)$.[31,32] The result shows that $\beta \sim +0.25$ for those CH_3 fragments with the highest recoil speed, in good agreement with $\beta = 0.3 \pm 0.05$ reported by Pino et al.[31] However, compared with their data, our fs-KETOF spectra exhibit a more prominent polarization effect because the slowest component (90 ps), which is expected to exhibit a zero anisotropy, is almost absent at $t = 1.0$ ps.

Using procedures described elsewhere,[24,37] we transformed the time-resolved KETOF spectra shown in Figure 5 into the corresponding CH_3 speed distributions, shown in Figures 6 and 7, with respect to the center-of-mass (COM) of DMSO. It is clear that the early time distributions are very different from the later ones. As shown in Figure 6A, near the zero delay time (<0.1 ps), the speed distributions appear to contain a single broad component that peaks at a low speed of about 1000 m/s and tails to about 4000 m/s. Between 0.1 and 0.35 ps, a higher-speed component peaking at about 2800 m/s begins to emerge while the low-speed component rapidly vanishes. From 0.35 to 1.0 ps, the high-speed component continues to grow and reaches a constant level at about 1.0 ps. Beyond 1.0 ps (Figure 7), the 2800 m/s component remains constant, but a low-speed component peaking at about 1400 m/s slowly appears and continues to grow until ~450 ps. On the basis of their temporal behavior, each speed component can be correlated to a corresponding temporal feature observed in CH_3 transients described in the previous section.

The low-speed component (1000 m/s) observed near the zero delay times (<0.1 ps) were found to be nearly identical to speed distributions measured with off-resonance probe wavelengths, and its temporal behavior agrees very well with the DI component observed in the 333 and 350 nm CH_3 transients (Figures 3B). Accordingly, we assigned the early time low-speed component (1000 m/s) to DI of the initial state and/or intermediate species. On the other hand, the temporal behavior of the high-speed component appearing within 0.1−1.0 ps is consistent with the rising behavior observed in the early-time CH_3 transients (Figure 3B) and can be ascribed to the neutral CH_3 fragments.

The early-time (<0.5 ps) speed distributions are complicated by the presence of the DI components which must be removed to reveal the true distributions of methyl products arising from neutral-state dissociation. We used the distribution at $t = -0.1$ ps as a reference and subtracted the DI contribution from speed distributions measured at other times according to the ratio between DI intensities at the corresponding times and at −0.1 ps as determined in the 350 nm off-resonance methyl transient. This procedure is based on two assumptions: (1) At $t = -0.1$ ps, the speed distribution is dominated by the DI component; and (2) the shape of the DI distribution is time invariant. The first assumption is justified because contribution from neutral-state dissociation is expected to be negligible at $t = -0.1$ ps. The second assumption is reasonable because ion fragmentation usually occurs in the cationic ground state with a time scale long enough to equilibrate the internal energy, and therefore, the CH_3^+ ion speed distributions arising from DI at a fixed total energy are expected to be independent of pump−probe delay time. A more convincing support to the second assumption is

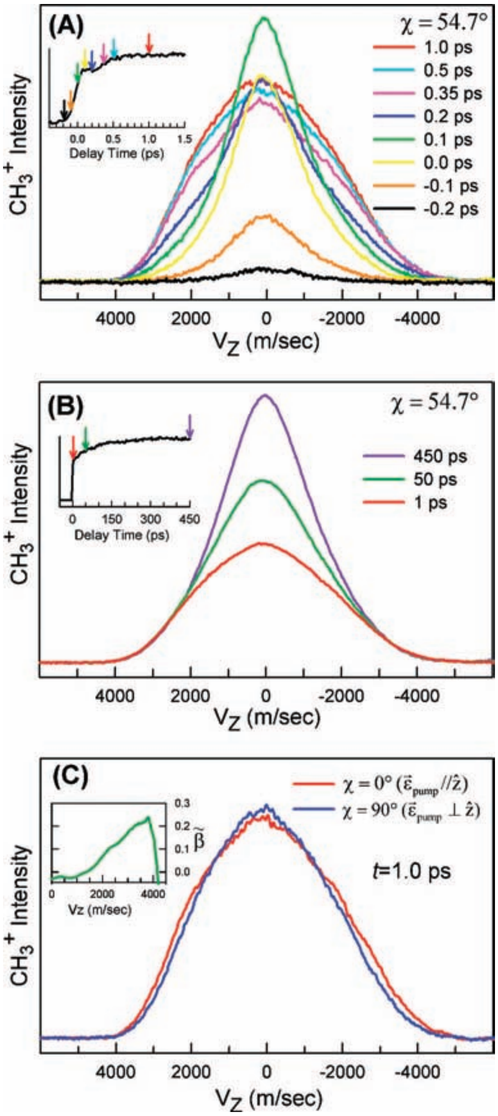

Figure 5. Femtosecond time-resolved CH_3 KETOF profiles measured at several delay times (A) between −0.2 and 1.0 ps and (B) between 1.0 and 450 ps with the pump-laser polarization oriented at $\chi = 54.7°$ with respect to the TOF-MS axis. The ion arrival time has been transformed into the fragment COM velocity along the TOF-MS axis (v_z). CH_3 transients measured under similar conditions are shown in the insets, and the solid arrows indicate the delay times at which KETOF spectra were recorded. (C) KETOF profiles measured at 1.0 ps with the pump-laser polarization being parallel and perpendicular to the TOF-MS axis. The inset shows the apparent anisotropy parameter as a function of v_z.

the observation of nearly identical shapes of the $t = -0.1$ and 0 ps distributions. The results of this DI subtraction procedure are shown in Figure 6B, which reveal the true speed distributions of neutral CH_3 fragments produced in the photodissociation of DMSO within 1.0 ps. Note that this correction procedure does not noticeably affect distributions beyond 0.35 ps where the DI contribution is negligible.

The shapes of the corrected speed distributions change with time, and the maxima slightly shift to the lower speeds at later times. More evidently, from 0.35 to 1.0 ps, the high-speed edges (>3200 m/s) are almost unchanged while the lower speed part increases significantly. Figure 6C shows the difference between the speed distributions measured at 1.0 and 0.35 ps, which represents the speed distribution of CH_3 fragments produced within this time interval. This time-difference speed distribution, which peaks at about 1900 m/s, is significantly different from the distribution measured at 0.2 ps, suggesting that a low-speed component is present at later times. These qualitative examinations clearly indicate that the speed distribution measured at 1.0 ps is actually composed of two components having distinct temporal behaviors and recoil speeds, a high-speed component that peaks at about 2800 m/s and rises sharply between 0 and ~0.35 ps and a low-speed component that peaks at about 1900 m/s and rises more slowly until about 1 ps. The speed distributions observed at 0.1 and 0.2 ps are predominated by the high-speed component, whereas the time-difference distribution (Figure 6C) between 0.35 and 1.0 ps mimics the low-speed component. These observations are consistent with the early-time CH_3 transient (Figure 3B) in which a complex temporal behavior is evident. Figure 6B also shows the fitting (solid lines) of the corrected speed distributions to a linear combination of two empirical speed distribution functions, $g(v) = A_1v^2\exp[-((v - v_1)/\sigma_1)^2] + A_2v^2\exp[-((v - v_2)/\sigma_2)^2]$, convoluted with a Gaussian instrumental function of 400 m/s (fwhm). The decomposed components at different delay times after deconvolution are shown in Figure 6D. The high-speed component peaks at ~3000 m/s at early delay times (<0.2 ps) and shifts to a slightly lower value of 2800 m/s at 0.35 ps and beyond. The maximum speed observed for this component is located at 4400 ± 100 m/s. The lower-speed component peaks at ~1900 m/s and resembles the time-difference distribution shown in Figure 6C.

Beyond 1 ps, the speed distributions (Figure 7) change much more slowly with time. The high-speed edges are nearly invariant, while a low-speed component peaking at about 1400 m/sec slowly grows in and reachws a constant level at about 450 ps. This clearly indicates that a low-speed component with a much slower rise time is present. The time-difference distribution between 1 and 450 ps is shown in Figure 7B and represents the speed distribution of the CH_3 fragment produced within this time window (1−450 ps). The temporal behavior of this low-speed component clearly indicates that it is associated with the 90 ps rise observed in the CH_3 transients.

3.4. The SO Transients. In the fs pump−LIF−probe experiments, the transient fluorescence signal was readily observed when the probe laser was tuned to SO B ← X transitions. A typical transient obtained with $\lambda_{pr} = 248.2$ nm for probing $SO(X^3\Sigma^-, v'' = 2)$ products via the B ← X (2,2) transition is shown in Figure 8A. Transient fluorescence measured by a digital oscilloscope as a function of time with respect to the probe-laser pulse at several pump−probe delay times are shown in Figure 8B. Analyses of these traces revealed that the lifetime of the major fluorescing species is ~21 ns, consistent with the literature value of the $SO(B^3\Sigma^-, v' = 2)$ collision-free lifetime of 27 ± 4 ns.[40] However, a very small component with a much longer decay time of ~270 ns was also observed in the fluorescence traces. Although the origin of this long-time fluorescence is not clear, it is certainly not due to the B ← X excitation of free SO because its lifetime is much too long.[40] Moreover, the integrator gate (50 ns width) used in our experiments highly discriminated against the long-time fluorescence component, and thus, it is not expected to cause significant interference to the pump−probe transients reported here. In fact, even around the zero pump−probe delay time where the long-lifetime fluorescence time component is most prominent (see the normalized plot in the Figure 8B inset), it accounts for only ~25% of the total signal in the pump−probe transients. Nevertheless, in order to reveal the true early-time dynamics, the long-fluorescence time contribution was removed

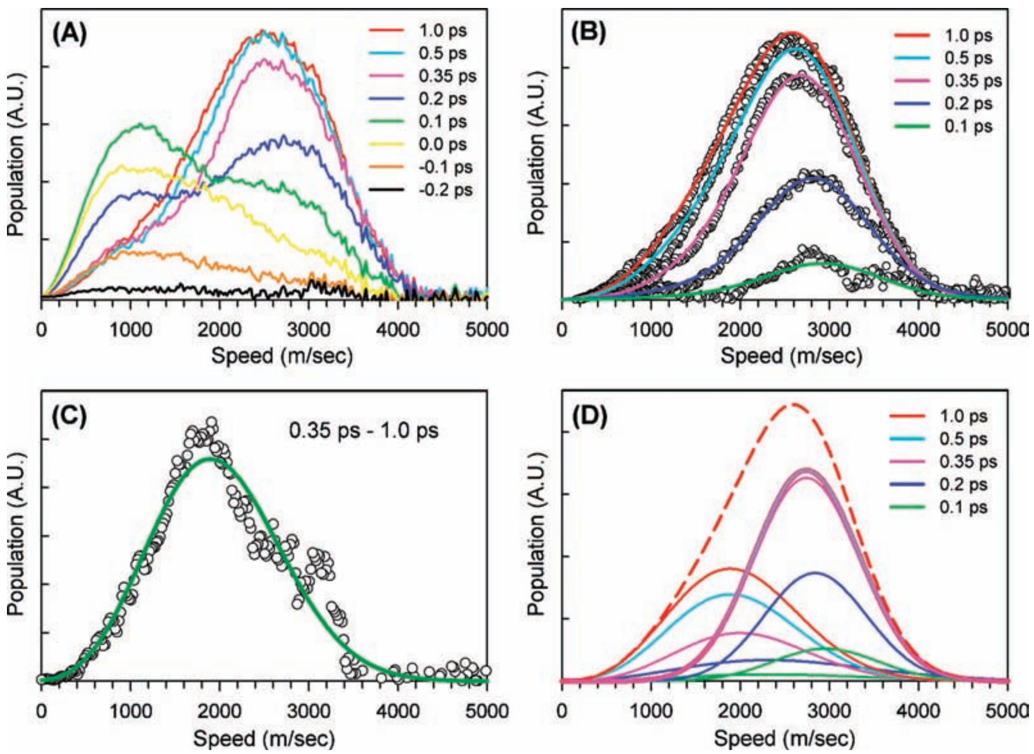

Figure 6. (A) Short-time-scale fs time-resolved speed distributions of CH_3^+, including those produced via ionization of neutral CH_3 fragments and DI of higher masses, with respect to the DMSO COM at several delay times between −0.2 and 1.0 ps. (B) Speed distributions of neutral CH_3 obtained by removing the DI component from distributions shown in (A) using the procedures described in the text. Open circles are the corrected data, and the solid curves are the best fit to a two-component model convoluted with a Gaussian response function of 400 m/s (fwhm). (C) Time-difference speed distribution obtained by taking the difference between distributions measured at 1.0 and 0.35 ps. (D) Deconvoluted components used to fit the distributions in (B). The dashed line is the best fit of the 1.0 ps distribution. Note that the high-speed component remains nearly unchanged beyond 350 fs.

by subtracting a weighted transient (Figure 8A inset) obtained with the same 50 ns integrator gate delayed by 200 ns (Figure 8B inset). The weighting factor was calculated according to a 270 ns exponential decay.

Figure 9 shows the transients obtained with the probe wavelength tuned to 241.5, 248.2, and 260.1 nm for probing $\upsilon'' = 1$, 2, and 3 vibrational levels of free SO(X) through SO B ← X (2,1), (2,2), and (1,3) transitions, respectively.[39−41] We assigned the observed transient fluorescence signal to the free SO(X) fragments arising from DMSO photodissociation on the basis of the following reasons: (1) the probe-wavelength dependence of the transient fluorescence signal is consistent with the reported LIF excitation spectra of nascent SO(X) produced in DMSO photolysis.[26,30] (2) The spectral filters used in the light collection system allowed only photons in the SO B → X fluorescence spectral region to enter the photomultiplier tube. (3) Laser-irradiance dependence studies indicated that the observed LIF transients are due to one-photon absorption of the pump and probe lasers. (4) The observed fluorescence lifetimes are ~21 ns throughout the entire transients, consistent with the literature values of SO B-state lifetimes.[40] This combined evidence unambiguously indicates that the observed transient fluorescence is due to free SO(X) produced in the DMSO photodissociation.

As shown in Figure 9, all fs pump−LIF−probe transients observed for SO(X) $\upsilon'' = 1$, 2, and 3 are characterized by a small, but very rapid, initial rise followed by a much larger, but slower, rise component. Nonlinear least-squares fits of these transients to a simple biexponential rise function convoluted with a Gaussian IRF of 250 fs (fwhm) gave a rise time of 50 ± 10 fs for the initial rapid rise. The rise times for the much slower component depend on the vibrational levels of SO(X) probed: 80 ps for $\upsilon'' = 1$, 42 ps for $\upsilon'' = 2$, and 23 ps for $\upsilon'' = 3$. The fast component makes up about 10−17% of all SO products observed. Because of the resonance LIF detection, free SO(X) can be observed only when the two C−S bonds break completely.[44,45] Thus, the SO transients observed here immediately suggest that there are at least two pathways leading to three-body dissociation.[46]

3.5. Electronic Structure Calculations. Electronic structure calculations relevant to the present study were carried out to aid in the interpretation of the experimental results. All calculations were carried out using the Gaussian 03 program package.[47] Only singlet states were calculated for DMSO because the extremely rapid initial-state decay and product rise within 1 ps imply that intersystem crossing is unlikely to play a role here.

3.5.1. The Initial State. Drage et al.[33] recently reported a high-resolution VUV absorption spectrum of vapor-phase DMSO. The absorption of DMSO starts at about 240 nm.[30,33] The first absorption band is weak and overlaps significantly with the second band.[30,33] Thorson et al.[30] have located the maximum of the first band at about 218 nm by means of spectral deconvolution. The second stronger band peaks at ~205 nm, which is followed by an even stronger band at about 188 nm.[33] Photoexcitation of DMSO at 200 nm in the present study thus excites mostly the 205 nm band. The general spectral features of these bands are broad and diffuse in character,[33] indicating that all states in this energy region are very short-lived. To further elucidate the nature of the initial state, we investigated

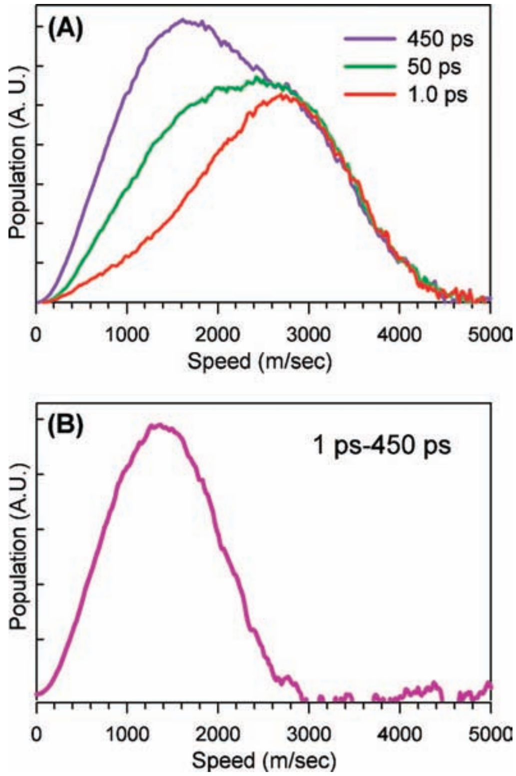

Figure 7. (A) Long-time-scale fs time-resolved speed distributions of neutral CH_3 fragments with respect to the DMSO COM at several delay times between 1.0 and 450 ps. (B) Time-difference speed distribution obtained by taking the difference between distributions measured at 450 and 1 ps.

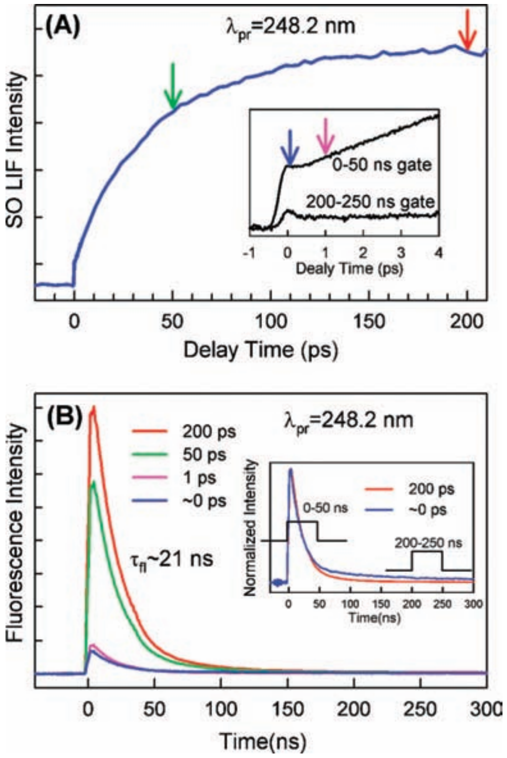

Figure 8. (A) A typical fs pump−LIF−probe transient with λ_{pr} = 248.2 nm. (B) Fluorescence signal measured at several pump−probe delay times indicated in the figure. The horizontal axis indicates the elapsed time relative to the probe-laser pulse. The inset in (A) shows the short-time-scale SO transients measured with two integrator-gate positions shown in the (B) inset. The one measured with the 200−250 ns gate has been multiplied by a weighting factor to reveal its magnitude as if it were measured with the 0−50 ns gate. Note that the two fluorescence traces shown in the (B) inset have been normalized.

the first few singlet excited states by means of electronic structure calculations. The ground-state structure of DMSO was first optimized at the MP4(SDQ)/6-311+G(d) level of theory, which gave a pyramidal structure that belongs to the C_s point group with the mirror plane passing through the S−O bond (see Figure 1). The vertical excitation energies at the optimized ground-state structure were then calculated at the TD-B3LYP/aug-cc-pVTZ level of theory for several singlet excited states. The results are summarized in Table 1 and Figure 10. Owing to the presence of the sulfur atom, the density of electronic states is rather high. The vertical excitation energies of the first four singlet excited states are found to lie in a small energy range of 0.7 eV. The calculated transition energies and oscillator strengths were used to simulate the VUV absorption spectrum reported by Drage et al.[33] by giving each transition an adjustable Gaussian band profile with area normalized to its oscillator strength. The result of the above procedure is far from acceptable. However, by shifting all transitions by about 0.6 eV higher in energy, a more satisfactory simulation can be attained, as shown in Figure 10. These shifted transitions are in good agreement with a recent report[48] on DMSO vertical excitation energy calculations using the coupled cluster linear response formalism (see Table 1). On these grounds, we assigned the 218 nm band to the $S_0 \rightarrow S_1(2^1A')$ transition, the 205 nm band to the $S_0 \rightarrow S_2(1^1A'')$ transition, and the 188 nm band to the $S_0 \rightarrow S_4(4^1A')$ transition. Accordingly, photoexcitation of DMSO at 200 nm in the present study most likely reaches the S_2 state. The transition dipole for $S_0 \rightarrow S_2(1^1A'')$ is perpendicular to the symmetry plane, while the others are in the plane. Our calculation also indicated that the S_2 state is primarily due to a HOMO(14a′) → LUMO + 1(8a″) excitation. Visual inspection and the constituent atomic orbital analyses suggested that the HOMO(14a′) bears π^*_{SO} and σ_{SC} characteristics, while the LUMO + 1(8a″) is better described as a mixture of σ^*_{SC} and some Rydberg orbitals. Thus, the S_2 state possesses some $\sigma_{SC}\sigma^*_{SC}$ characteristics, which is consistent with the rapid dissociation dynamics observed in this study.

3.5.2. Potential Energy Surface Scan. We calculated potential energy curves along some relevant dissociation coordinates using the following general procedures. First, the coordinate of interest, for example, the C−S bond distance, was scanned while all remaining coordinates were optimized for the ground state at the B3LYP/6-311G(d) level of theory. The ground-state energy at each optimized structure was then recalculated at the UQCISD(T)/6-311G(d) level in order to construct the ground-state minimum-energy path (MEP). The vertical excitation energies of several singlet excited states at each optimized structure along the ground-state MEP was then calculated at the TD-B3LYP/6-311++G(3df,2p) level of theory. Note that the excited-state potential energy curve thus obtained is merely a cross section of the global excited-state potential energy surface along the calculated ground-state MEP.

(1) Ground-State and Excited-State Umbrella Inversion. The equilibrium structure of ground-state DMSO assumes a C_s pyramidal geometry. Using the procedures described above, we have investigated the ground-state and excited-state energies along the umbrella inversion coordinate from $\alpha = 90$ to 0°. The results, summarized in Figure 11, indicate that the equilibrium angle is about 64.7° in the ground state. Unlike all other states calculated, the S_1 state was predicted to have a minimum at the planar configuration ($\alpha = 0°$), consistent with the results reported by Cubbage et al.[49] using CASSCF. This suggests that once DMSO is in the S_1 state via a vertical transition from other

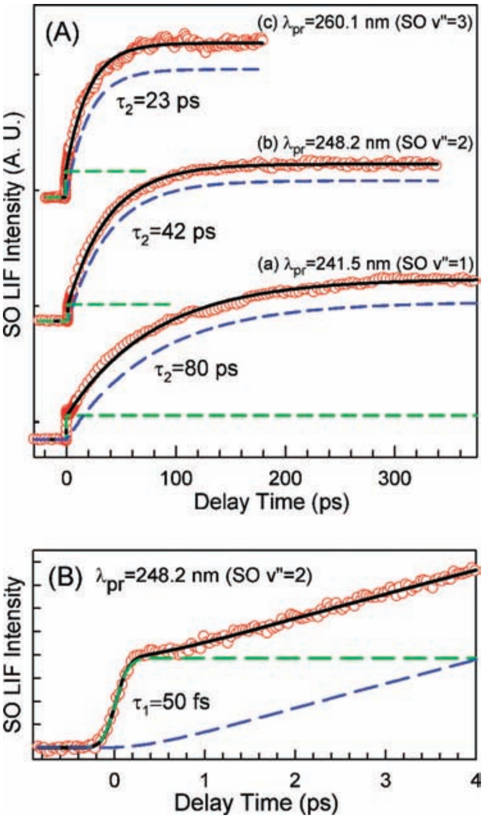

Figure 9. (A) Long-time-scale fs pump−LIF−probe transient at three different probe wavelengths for probing SO (X) v'' = 1, 2, and 3 products. The black solid lines are the best fits, and the dashed lines are the decomposed components. The data have been normalized and shifted vertically for clarity. (B) Enlarged short-time-scale view of the 248 nm transient shown in (A). The long-lifetime fluorescence time component described in the text has been removed.

TABLE 1: Vertical Excitation Energies of the Four Lowest Singlet Excited States in DMSO

	this work			Mondéjar et al[a]		
state	ΔE (eV)	f[b]	symmetry	ΔE (eV)	f[b]	symmetry
S_4	6.02	0.0827	A′	6.73	0.0925	A′
S_3	5.70	0.0084	A′	6.13	0.0208	A′
S_2	5.55	0.0467	A″	6.09	0.0584	A″
S_1	5.32	0.0136	A′	5.90	0.0030	A′

[a] Ref 48. [b] Oscillator strength.

states, it should undergo a large-amplitude umbrella inversion motion. This motion plays an important role in the dissociation mechanism discussed below.

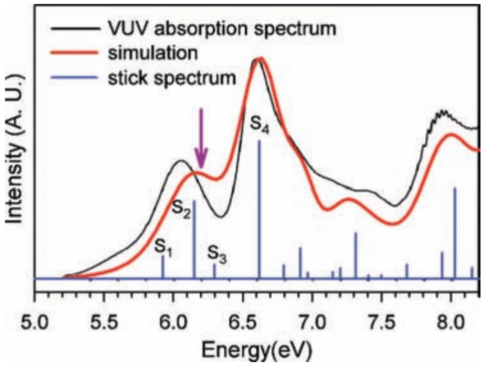

Figure 10. Stick spectrum and spectral simulation using the shifted vertical excitation energies as described in the text. The experimental absorption spectrum is taken from ref 33, and only the energy range between 5.2 and 8.0 eV is shown. The arrow indicates the excitation energy in this work.

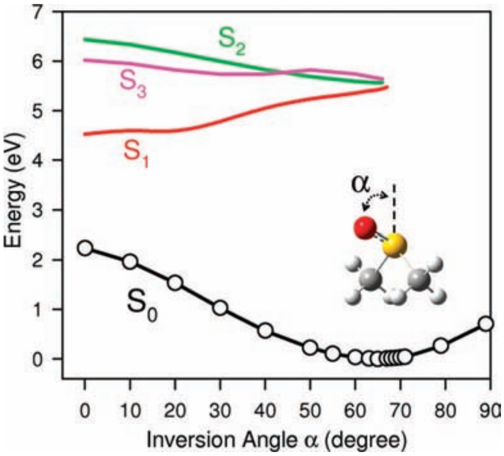

Figure 11. Calculated potential energy curves along the ground-state MEP for umbrella inversion motion in DMSO.

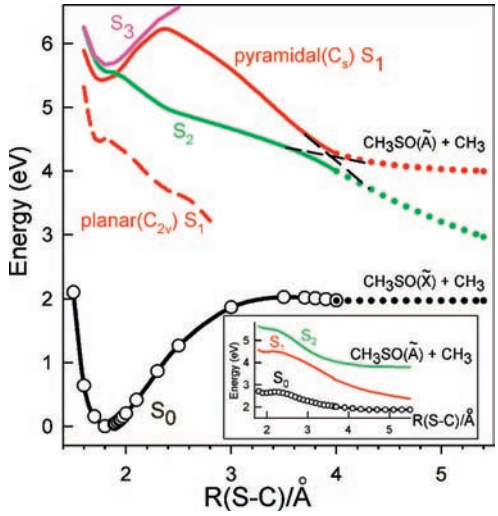

Figure 12. Calculated potential energy curves along the ground-state MEP for the breaking of one S−C bond in DMSO. The dotted lines were obtained without ground-state geometry optimization. The dashed line is the S_1 state energy curve under a planar geometric restriction (C_{2v}). The inset shows the energy curves for S_0, S_1, and S_2 states calculated with the C−S−C angle fixed at a large value of 160°.

(2) Primary S−C Dissociation. Potential energy curves of the ground state and several excited states along the primary S−C dissociation coordinate were also calculated. Twenty C−S bond distances ranging from 1.6 to 4 Å were calculated in order to obtain the potential energy curves shown in Figure 12. Asymptotic behaviors beyond 4 Å (dotted line) were evaluated by simply calculating energies at the corresponding S−C bond lengths with other coordinates optimized at R(S−C) = 4 Å. This procedure gave a ground-state S−C bond energy of 190 kJ/mol (1.97 eV), slightly lower than the thermochemically determined value (214 J/mol).[34] Near the ground-state equilibrium position, the S_1, S_2, and S_3 states lie very closely in energy. Along the ground-state C−S bond dissociation MEP, the S_1 state is predicted to be predissociative with a relatively high barrier of about 1 eV. On the other hand, the S_2 state is strongly repulsive and correlates diabatically to an electronically excited product, $CH_3SO(\tilde{A})$. An avoided crossing between the S_2 and S_1 states along the coordinate shown in Figure 12 can be inferred. However, at other geometries with nearly planar structures or large C−S−C angles (see Figure 12 inset), the S_2

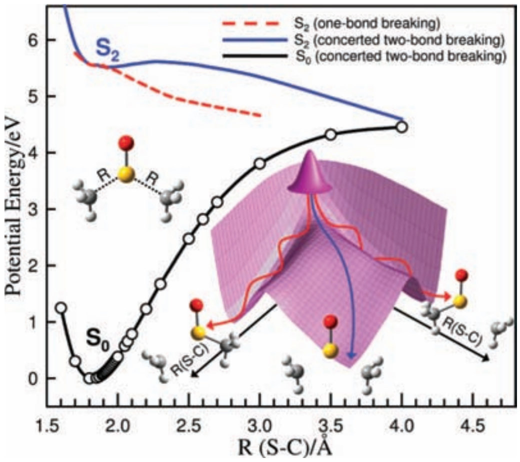

Figure 13. Calculated potential energy curves along the ground-state MEP for the concerted breaking of two C−S bonds in DMSO. For comparison, the potential energy curve for one C−S bond breaking (dashed line) is also shown. The inset is a schematic S_2-state potential energy surface based on the calculated results, and the wiggled arrows are conjectured reaction trajectories for the concerted (blue) and stepwise (red) dissociation.

state is found to adiabatically dissociate into $CH_3SO(\tilde{A})$. The S_3 and S_4 states are found to be adiabatically bound with respect to S−C bond breaking in all conformations studied. Combined with the diffuse absorption spectrum of DMSO in the $S_0 \rightarrow S_3/S_4$ region, this finding suggests that the S_3 and S_4 states are probably strongly coupled with the repulsive S_2 state. Similar procedures were also carried out for the S_1 states under a geometric restriction in which the four heavy atoms and a hydrogen atom from each methyl group were confined in the same plane. The result is also depicted in Figure 12 (dashed line). Interestingly, the planar S_1 state, which is lower in energy than the pyramidal form (see Figure 11), is strongly repulsive along the S−C coordinate! This result is consistent with the fact that the absorption spectrum in the $S_0 \rightarrow S_1$ region is broad and diffuse.

(3) Concerted Two S−C Bond Dissociation. We also investigated the potential energy curves for the concerted breaking of the two equivalent C−S bonds. The procedures are the same as those above, except that in this case, the lengths of the two C−S bonds were scanned simultaneously, that is, both S−C bond lengths are identical at each point of the curve and the C_s symmetry is maintained throughout, while all remaining coordinates are optimized. The results are shown in Figure 13 for S_0 and S_2 states. Along the ground-state concerted dissociation MEP, the S_2 state exhibits a generally repulsive profile with a very low barrier. Note that this curve is merely a cross section of the global potential energy surface (PES) along the ground-state MEP. It is likely that a purely repulsive pathway toward concerted dissociation may exist on the S_2 surface. As mentioned in the previous section, the S_2-state PES along the ground-state single C−S bond dissociation MEP is also repulsive (see Figure 12) with an even steeper slope and can lead to an electronically excited CH_3SO. Therefore, the S_2 PES is generally repulsive for the breakage of the two equivalent C−S bonds. A schematic PES of the S_2 state is shown in the Figure 13 inset to illustrate the surface topology along the two C−S bonds.

(4) S−C Dissociation and C−S−O Bending in CH_3SO. At the excitation energy used in this work, it is energetically feasible to break the two S−C bonds. Accordingly, the reaction intermediate, the CH_3SO radical, plays a crucial role in the overall dissociation dynamics. We studied the CH_3SO ground state and the first excited state ($\tilde{A}^2A''$) along the S−C dissociation and C−S−O bending coordinates using the same procedure as described above, except that the ground-state optimizations were done at the UB3LYP/6-311++G(3df,2p) level of theory. The results are summarized in Figure 14. Our results indicate that the bond energy of CH_3−SO is about 2.2 eV (213 kJ/mol), consistent with the thermochemical data.[34] No exit barrier along the $CH_3SO(\tilde{X})$ C−S dissociation MEP was identified at the level of theory employed here. The $\tilde{A}^2A''$ state was also found to be adiabatically bound with respect to the C−S dissociation. The minimum of the $\tilde{A}^2A''$ state was calculated at the TD-UB3LYP/6-311++G(3df,2p)//CIS/6-311++G(3df,2p) level of theory and was found to lie at about 2.04 eV (197 kJ) above the ground state.

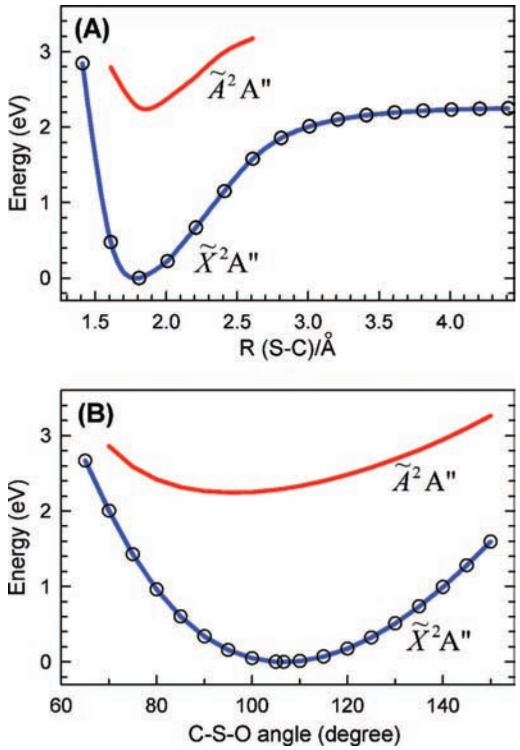

Figure 14. (A) Calculated potential energy curves along the ground-state MEP for the breaking of the C−S bond in CH_3SO. (B) Calculated potential energy curves along the ground-state MEP for the C−S−O bending motion in CH_3SO.

In the C−S−O bending coordinate, it was found that the equilibrium angle in the ground state is about 106°, whereas the $\tilde{A}$ state seems to favor a smaller angle. Near the ground-state equilibrium angle, the two states are separated by about 2 eV. However, as the C−S−O angle decreases, the two states move closer and cross at a small angle. This crossing may promote a rapid internal conversion from $CH_3SO(\tilde{A})$ to $CH_3SO(\tilde{X})$.

4. Discussion

The experimental results presented here have revealed the temporal evolution of the initial state, intermediates, and final products (CH_3 and SO) for the photodissociation of DMSO at 200 nm. Some descriptive conclusions can be drawn readily. The parent (DMSO) transient indicates that the initial state prepared by 200 nm excitation is extremely short-lived, that is, about 30 fs. According to our calculations (see section 3.5.1), the initial fs excitation at 200 nm launches a nuclear wave packet on the S_2 surface. The repulsive nature of the S_2 state and the close vicinity of S_2 and S_1 suggest that adiabatic and nonadiabatic dynamics occur rapidly and competitively. The observed parent transient is consistent with this picture and indicates that these rapid initial steps take place in about 30 fs to move the system out of the probing window.

After the initial steps, the dynamics is manifested by the temporal evolution of the SO and CH_3 products. The biphasic behavior observed in the SO transients indicates that there are at least two SO components, a minor "fast SO component" that rises nearly instantaneously in about 50 fs and a major "slow SO component" that rises much more slowly in 20−80 ps, depending on the vibrational level of SO(X) probed. The CH_3 transients and fs time-resolved CH_3 speed distributions reveal that there are *at least* three major CH_3 product components, (1) a "fast CH_3 component" that rises rapidly with a coherent delay of 130 fs and is associated with a high-speed distribution centered at about 2800 m/s, (2) a "medium CH_3 component" that rises in about 350 fs and is accompanied by a speed distribution centered at about 1900 m/s, and (3) a "slow CH_3 component" that rises much more slowly in about 90 ps and exhibits a speed distribution that peaks at a much lower speed of 1400 m/s. Notably, Blank et al.[27] and Pino et al.[31] have also identified three CH_3 components characterized by similar speed distributions. In the following, we will begin by discussing the dynamical features reveled in these product channels together with a theoretical support from the electronic structure calculations. Comparisons with previous reports in the literature will also be discussed.

4.1. The Fast SO Component. The small instantaneous rise observed in the SO transients indicates that a small fraction of SO is produced nearly instantaneously in about 50 fs! Because of the resonance LIF detection, free SO can be observed only when the two C−S bonds break completely. Two possible mechanisms are considered to account for the nearly instantaneous appearance of SO products. The first one is similar to the molecular elimination channel occurring in the photodissociation of formaldehyde[50] and carbonyl cyanide.[8] In such a case, SO and C_2H_6 are produced through a three-center transition state. However, such molecular channels usually occur in the ground state with a very high barrier and are expected to occur very slowly, which is certainly not consistent with the nearly instantaneous rise. Moreover, no observation of C_2H_6 has ever been reported in previous PTS experiments with more universal detections.[27,29,30] We therefore dismissed the molecular channel as the origin of the fast SO component.

The second possible mechanism involves a rapid breaking of the two equivalent C−S bonds in a concerted fashion or in a rapid succession in about 50 fs. This is possible if the excited-state surface involved is repulsive along the two-bond dissociation coordinate. On the basis of previous[27,29] and our own product speed distribution measurements, we estimated the terminal relative speed of C−S separation to be no greater than 5500 m/s.[51] Therefore, the 50 fs time period is merely enough to extend one C−S bond by 2.75 Å at most to become about 4.55 Å, at which the bond can be considered as broken. Thus, the observation of the nearly instantaneous appearance of free SO products in 50 fs suggests that the two C−S bonds must break almost simultaneously within 50 fs, that is, a concerted three-body dissociation. It is important to note here that our observation does not assert a synchronously concerted three-body dissociation mechanism. It is possible that the bond breaking occurs in an asymmetric fashion such that the "dissociating intermediate", CH_3−SO, is under the influence of the leaving counter fragment, CH_3, and hence the dynamics of the entire dissociating complex, CH_3−S(O)−CH_3, is governed by the three-body potential.

This assignment is supported by our theoretical results shown in Figure 13. As mentioned earlier, the S_2 PES is repulsive for the breakage of the two equivalent C−S bonds. Along the concerted two-bond dissociation coordinate, the S_2 state exhibits a generally repulsive profile with a zero or very low barrier. A schematic PES of the S_2 state is shown in the Figure 13 inset. The initial wave packet is launched on the S_2 surface at the ground-state equilibrium geometry (pyramidal) along the diagonal direction. The topology of the S_2 surface suggests that, although the majority of the trajectories will go asymmetrically and result in breaking of a single C−S bond, a small fraction of trajectories may slide into the diagonal region and lead to a concerted, but not necessarily synchronous, breaking of the two C−S bonds. Thus, both concerted and stepwise trajectories are present, and the branching is determined by the S_2 surface topology and by the initial motion of the wave packet. The reactive trajectories leading to the concerted three-body dissociation are simply out numbered by those leading to stepwise dissociation. This description is consistent with the small amplitude of the 50 fs rise observed in the SO LIF transients.

Additional experimental support for the competing concerted and stepwise dissociation comes from the photodissociation of tetramethylene sulfoxide (TMSO) that has been reported previously.[46] Upon photodissociation at 200 nm, TMSO gives a much larger instantaneous (50 fs) SO rise. In TMSO the two C−S bonds are linked together with an alkyl chain, and therefore, the dissociation of a single C−S bond is somewhat hindered by the chain constraint and becomes less repulsive. This constraint does not exist in the concerted pathway, making it more competitive and resulting in a larger branching ratio, as observed. This example demonstrates that the branching between the concerted and stepwise pathways can be controlled chemically.

4.2. The Slow SO Component. The rise times of the slow SO component depend on the vibrational level of SO(X) probed and range from 80 to 20 ps, indicating that a much slower dissociation pathway is also present. Because the slow component amounts to ~90% of the observed SO signal, it must be due to a major SO-producing channel besides the above-mentioned concerted three-body dissociation. Accordingly, the molecular channel leading to SO and C_2H_6 is not likely to be responsible for the slow component because it would imply a very low CH_3 quantum yield, which apparently contradicts the experimental observations.[27−31] On the other hand, the slow SO rise is consistent with a secondary decomposition of hot CH_3SO produced in the stepwise pathway that competes favorably with the concerted three-body dissociation. This assignment is consistent with most previous studies which concluded that the reaction mainly proceeds through a stepwise mechanism and that the CH_3 quantum yield is high.[27−31] The C−S bond energy in CH_3SO is relatively high[27,29] (see section 3.5.2), and therefore, the secondary decomposition is expected to proceed slowly even if a high vibrational energy is deposited in the intermediate. We have carried out variational RRKM calculations to estimate the decomposition rates of CH_3SO containing a reasonable range of vibrational energies and found them to be consistent with the observed slow SO rise times (see below). The product vibrational level dependence of the slow SO rise is rather interesting and will be discussed in details below.

4.3. The Fast CH_3 Component. The fast CH_3 component rises almost instantaneously with a coherent delay of about 130 fs and is associated with a speed distribution that peaks at about 2800 m/sec and tails to a maximum speed of about 4400 m/s.

The temporal behavior unequivocally indicates that this component is due to a direct dissociation on a purely repulsive surface.[11,12] This assignment is supported by our electronic structure calculations, which indicated that the initially excited S_2 state is repulsive along the one-bond S$-$C dissociation coordinate. Such a prompt dissociation is expected to result in an anisotropic recoil velocity distribution. As mentioned earlier, the transition dipole of the initial excitation ($S_0 \rightarrow S_2(1^1A'')$) is perpendicular to the symmetry plane. On the basis of the DMSO ground-state structure (C_s), the angle between the transition dipole and the recoiling C$-$S bond is predicted to be about 42°, giving an anisotropy parameter (β) of 0.65 in the limit of prompt dissociation.[52] Our anisotropy measurement shown in Figure 5C indicates that the fragments with the highest speed indeed recoil with a noticeable anisotropy of $\beta \sim +0.25$. The slightly lower observed anisotropy could result from either vibrational smearing or structural distortion upon excitation. Note that the positive β value observed here does not support a transition dipole parallel to the SO moiety[27,31,32] because it would result in a negative anisotropy under the pyramidal structure.

One seemingly possible origin of the fast CH_3 component is the concerted three-body dissociation discussed earlier because it should produce a corresponding CH_3 component with a rapid temporal behavior similar to the fast CH_3 component. However, the small fraction ($<10\%$)[53] of CH_3 produced in the concerted dissociation estimated from the SO transient is not consistent with the relatively large amplitude ($>30\%$) observed for the fast CH_3 component. Moreover, a simple kinematic calculation using the ground-state structure and the available energy at 200 nm excitation predicted a maximum CH_3 speed of only $\sim$2900 m/s for the concerted three-body dissociation, much lower than the observed maximum speed of 4400 m/s. Thus, we concluded that the majority of the fast CH_3 component is not due to the concerted three-body dissociation; instead, it must arise from a primary C$-$S direct dissociation leading to $CH_3SO + CH_3$ (fast). Nevertheless, the above considerations indicate that CH_3 produced in the concerted three-body dissociation should exhibit a temporal behavior similar to the fast CH_3 component and a speed distribution partially overlapped with those of the fast and medium CH_3 components. These entangled behaviors and its relatively low amplitude make the concerted pathway difficult to be resolved in the CH_3-probing experiments.

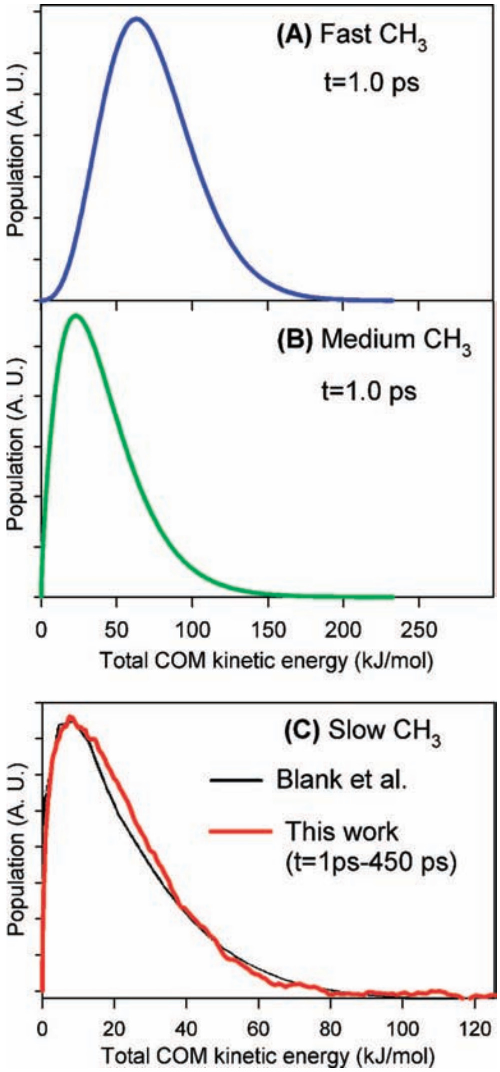

Figure 15. Total KEDs in the DMSO COM frame for primary dissociations associated with the (A) fast CH_3 and (B) medium CH_3 components derived from their corresponding deconvoluted distributions at 1.0 ps shown in Figure 6D. (C) Total KED in the DMSO COM frame derived from the speed distribution of the slow CH_3 component shown in Figure 7B as if it were due to a primary dissociation. Also shown for comparison is the low-energy component reported by Blank et al. (taken from ref 27).

The total kinetic energy distribution (KED) derived from the fast CH_3 component at $t = 1$ ps for the reaction $DMSO^* \rightarrow CH_3SO + CH_3$ (fast) is shown in Figure 15A. The average total kinetic energy release in this reaction is about 70 kJ/mol, or only about 18% of the available energy (384 kJ/mol), and the maximum kinetic energy release is 180 ± 10 kJ/mol. Because direct dissociation occurring on a repulsive surface is expected to partition a large fraction of available energy into translational degrees of freedom, the low $\langle f_{tr} \rangle$ determined here for the fast CH_3 component suggests that the corresponding dissociation may lead to electronically excited fragments. This speculation is supported by our calculations, which indicate that the S_2 state can dissociate to produce $CH_3SO(\tilde{A})$, which lies at 2.04 eV (197 kJ/mol) above its ground state. The observed maximum kinetic energy of 180 kJ/mol implies that the CH_3SO excited state lies at 204 kJ/mol, consistent with the theoretical prediction.

Blank et al.[27] have also resolved a similar high-energy component in their PTS experiment using tunable vacuum UV radiation for product ionization and 193 nm for photolysis. The total KED that they derived for the fast primary dissociation channel peaks at about 100 kJ/mol and tails to about 175 kJ/mol. Thus, the CH_3 $v = 0$ selected KED measured in this work is roughly similar to that obtained with more universal detection. A comparison for the low-energy component discussed below shows an even closer resemblance (Figure 15C). The similarity between the $v = 0$ selected KEDs and those measured with more universal detection suggests that the CH_3 products are not highly vibrationally excited, and therefore, the CH_3 $v = 0$ KED is a good representative to all methyl fragments. In fact, Rudolph et al.[28] reported that 30% of methyl products are produced in the vibrationless level, and Pino et al.[31] reported that the average vibrational energy in the CH_3 ν_2 mode is only about 10 kJ/mol. Moreover, because the counter fragment (CH_3SO) may accommodate a great portion of the available energy, vibrationally cold CH_3 is not necessarily correlated with higher kinetic energy, and the KED may be quite robust regardless of the CH_3 vibrational state selected.[24]

Blank et el.[27] and Pino et al.[31] have also assigned this high-energy component to a pathway producing electronically excited CH_3SO. These authors have suggested that the resulting electronically excited CH_3SO would undergo radiative relaxation to form cold $CH_3SO(\tilde{X})$, which does not decompose. However, we did not observe any noticeable fluorescence in our LIF experiments when only the pump laser (200 nm) was present and the bandpass filters were removed. To elucidate the evolution of the intermediate species, we have measured the CH_3SO transients, as shown in Figure 2B. The CH_3SO transient contains, in addition to a DI component arising from DMSO initial state, an intermediate component (blue dashed line), with the rise and decay times being about 30 and 80 fs, respectively. Because both $CH_3SO(\tilde{A})$ and $CH_3SO(\tilde{X})$ are adiabatically bound with respect to C−S bond breaking (see Figure 14A), it is unlikely that such a fast decay is the result of secondary decomposition. We proposed that this component is due to a fast internal conversion of $CH_3SO(\tilde{A})$ to $CH_3SO(\tilde{X})$. This speculation is supported by our electronic structure calculation. As shown in Figure 14B, the potential energy curves of $CH_3SO(\tilde{A})$ and $CH_3SO(\tilde{X})$ along the MEP for the C−S−O bend show a possible crossing at a smaller angle. It is plausible that the two surfaces may cross at a configuration near the excited-state minimum such that internal conversion can be effectively promoted via the C−S−O bending motion. The CH_3SO ground state thus produced is internally very hot and can undergo secondary decomposition, as discussed below.

4.4. The Medium CH_3 Component. The medium CH_3 component rises in about 350 fs and associates with a speed distribution that peaks at about 1900 m/s. Blank et al.[27] and Pino et al.[31] have also reported a similar component and attributed it to the secondary dissociation of hot CH_3SO intermediate following a DMSO S_0-state primary dissociation. However, because the C−S bond energies in DMSO S_0 and $CH_3SO(\tilde{X})$ are relatively large, the 350 fs rise time observed in this work does not support this assignment. Furthermore, we did not observe a corresponding component in the SO transients that can be correlated with the 350 fs CH_3 rise. Accordingly, we ascribed this component to another primary C−S dissociation that produces CH_3 and hot CH_3SO radicals. The total KED at $t = 1$ ps derived for the reaction producing this component, that is, $DMSO^* \rightarrow CH_3SO + CH_3$(medium), is shown in Figure 15B.

One seemingly possible pathway for producing such a component is the DMSO S_0 dissociation following a fast internal conversion from the initially excited S_2 state. However, the C−S bond energy in DMSO S_0 is as high as 214 kJ/mol, and therefore, the decomposition is expected to proceed slowly. We have performed a variational RRKM calculation for DMSO S_0 dissociation at an energy equivalent to 200 nm excitation. The results gave a dissociation time on the order of a few picoseconds, which is not consistent with the observed much faster rise of 350 fs. Moreover, the total KED of the medium CH_3 component does not peak at near zero as expected for ground-state dissociation. Indeed, it is very different from the prior distribution predicted by Blank et al.[27] for DMSO S_0 dissociation. These combined considerations led us to exclude the S_0 dissociation channel for the medium CH_3 component.

In view of all experimental and theoretical results, we proposed that the medium CH_3 component is most likely due to the S_1-state C−S dissociation following a rapid internal conversion from the initially excited S_2 state. This assignment is based on the following reasons: (1) The S_2 and S_1 states lie very closely in energy, and therefore, $S_2 \rightarrow S_1$ internal conversion is expected to be extremely fast. (2) The broad and continuous absorption in the $S_0 \rightarrow S_1$ spectral region[33] indicates that the S_1 state is indeed very short-lived. (3) Our calculations suggest that the DMSO S_1 state favors a planar structure in which the C−S bond becomes repulsive. (4) The average speed of the counter fragment, CH_3SO, can be predicted by momentum matching to be about 450 m/sec, which is not inconsistent with the time-of-flight spectra of CH_3SO and CD_3SO reported by Zhao et al.[29] and Blank et al.,[27] respectively.

In this S_1-state C−S primary dissociation pathway, the average total kinetic energy release is only about 34 kJ/mol, or about 9% of the available energy, indicating a high internal excitation in the fragments. We believe that this is due to the large difference between the initial-state and S_1-state geometries. The initially excited S_2 state is launched at the ground-state equilibrium structure, which is pyramidal and has a C−S−C bond angle of about 97°. The sudden conversion from S_2 to the S_1 state, which favors a planar geometry and a much larger C−S−C angle,[49] immediately induces large-amplitude vibrational motions along these coordinates. Thus, a very large fraction of the available energy in the S_1 state is initially deposited in a few modes other than the repulsive S−C coordinate, and the kinetic energy release is thus very limited. According to the energy curves shown in Figure 12, after ultrafast $S_2 \rightarrow S_1$ IC, the available energy localized in the C−S dissociation coordinate is no greater than 240 kJ/mol, and the rest is localized in the umbrella inversion motion. This value is an upper limit because the S_1 potential energy curve under planar restriction shown in Figure 12 is not the true MEP on the S_1 surface. Geometric changes in other coordinates, such as the C−S−C bend and SO stretch, can further reduce the available energy initially localized in the C−S coordinate to a much lower value and therefore give a lower kinetic energy release. The unique topology of the S_1 surface also explains the relatively slow dissociation of about 350 fs. As mentioned above, upon $S_2 \rightarrow S_1$ internal conversion, the molecule immediately executes a large-amplitude umbrella inversion motion. The repulsive part of the S_1 surface is accessed only when the vibrating molecule passes through the planar structure region. This unique dynamical behavior effectively retards the dissociation to about 350 fs and allows the system to further redistribute some of the energy initially localized in the C−S coordinate into other modes.

4.5. The Slow CH_3 Component. The slow CH_3 component rises in about 90 ps and is associated with a speed distribution peaking at a low value of about 1400 m/s. Assuming that it arises from a primary C−S dissociation, the total KED derived from this component was found to be very similar to the low-energy component reported by Blank et al.,[27] as shown in Figure 15C. At first glance, this seems to suggest that the slow CH_3 component is due to the DMSO ground-state C−S primary dissociation as proposed by these authors.[27,31] However, the similar time scales observed for the slow CH_3 (90 ps) and slow SO (80−25 ps) components also strongly imply that they are correlated, that is, both are the result of the secondary decomposition of hot CH_3SO. The slow SO component observed in the LIF experiment indicates that a slow secondary dissociation of hot CH_3SO is present, and therefore, there must be a corresponding CH_3 component appearing on the similar time scale. If the slow CH_3 component was due to the DMSO ground-state primary dissociation, which does not produce SO, it would be difficult to reconcile the slow SO component with the observed CH_3 transients. Moreover, the very low kinetic energy associated with the slow CH_3 component is indeed perfectly consistent with hot CH_3SO decomposition. We have also carried out variational RRKM calculations to provide additional support. The calculations predicted that DMSO S_0 dissociation at 200 nm excitation proceeds on a time scale of a few picoseconds due to the high internal energy and its relatively small molecular size. On the basis of this reasoning, we excluded the DMSO S_0

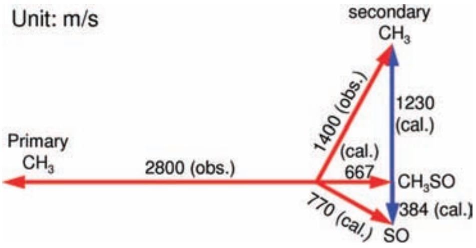

Figure 16. Newton diagram showing the relationships between the fragment average velocities in the parent (DMSO) COM frame (red arrows) and that in the intermediate (CH_3SO) COM frame (blue arrows).

dissociation channel and assigned the slow CH_3 component to the secondary dissociation of hot CH_3SO. The seeming disagreement between the slow CH_3 rise time (90 ps) and that of high-v'' ($v'' = 2$ and 3) SO will be explained in the next section.

As discussed above, there are two primary dissociation channels that can produce hot CH_3SO. In the one that produces the medium CH_3 component, that is, the S_1-dissociation channel, the average total kinetic energy release has been estimated to be about 34 kJ/mol. Assuming that the rest of the available energy is equally partitioned into all other degrees of freedom of the two primary products, the resulting hot CH_3SO would contain an average vibrational energy of about 180 kJ/mol, which is 40 kJ/mol lower than the energy needed to break the C−S bond in CH_3SO. Although this prediction should be used with caution because the DMSO S_1 dissociation is likely to be nonstatistical, it does suggest that only a fraction of hot CH_3SO produced in this channel can undergo secondary dissociation. On the other hand, the primary dissociation giving rise to the fast CH_3 component, that is, the S_2-dissociation channel, leads to $CH_3SO(\tilde{A})$, which is expected to undergo a rapid internal conversion to produce much vibrationally hotter $CH_3SO(\tilde{X})$ (see section 3.5.2(4)). The CH_3SO thus produced should contain the $\tilde{A}-\tilde{X}$ electronic energy plus the internal energy acquired during the primary dissociation. Because the $\tilde{A}-\tilde{X}$ energy difference (∼200 kJ/mol) is close to the $CH_3SO(\tilde{X})$ C−S bond energy (220 kJ/mol), the hot $CH_3SO(\tilde{X})$ produced in the S_2 primary dissociation should almost all contain enough energy to decompose. A canonical averaging of RRKM rates[54] over a CH_3SO vibrational energy distribution derived from the total KED for the S_2 dissociation (Figure 15A) gave an average time constant of about 70 ps. Although the excellent agreement with the slow component is probably just a coincidence because CH_3SO intermediates produced in the S_1-dissociation channel were not included, it does provide an order-of-magnitude support to our assignment. The above description is also consistent with the CH_3SO transients shown in Figure 2B. In addition to a CH_3SO $\tilde{A} \rightarrow \tilde{X}$ internal conversion component mentioned earlier, a small and much slower component (see Figure 2B inset) that can be ascribed to the temporal evolution of hot $CH_3SO(\tilde{X})$ is evident and is consistent with an incomplete slow secondary dissociation described here.

According to this assignment, the speed distribution of the slow CH_3 component must be reanalyzed in the three-body frame. Assuming that the primary and secondary dissociations are nearly isotropic, a very simple procedure[20] can be applied to approximate the three-body dissociation kinematics, as shown in Figure 16. The average COM speeds of the fast and slow CH_3 components were used for this purpose. This simple procedure yields an average kinetic energy release of only about 15 kJ/mol for the secondary dissociation in the CH_3SO frame, in accordance with the slow hot $CH_3SO(\tilde{X})$ decomposition. This analysis also gives an average COM speed of SO (in the DMSO frame) of about 770 m/s, which is consistent with the raw SO TOF spectra reported by Blank et al.[27]

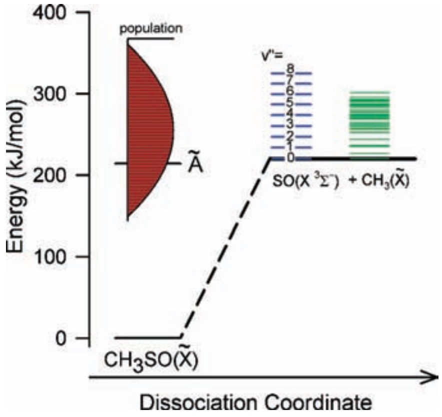

Figure 17. Schematic energy level diagram showing the relevant reactant and product states for the decomposition of CH_3SO. The product vibrational levels of SO and CH_3 are drawn to scale as harmonic oscillators. Also shown in the diagram is a conjectured vibrational energy distribution of hot CH_3SO (red shaded area) resulting from the primary dissociation discussed in the text.

4.6. Product Vibrational-Level Dependence of the Slow SO Component. One rather interesting observation in this work is the product vibrational-level dependence of the slow SO rise times: 80 ps for $v'' = 1$, 42 ps for $v'' = 2$, and 23 ps for $v'' = 3$. Although the vibrationless SO($v'' = 0$) was difficult to measure accurately due to the small Franck−Condon factor[55] and spectral congestion, it is reasonable to estimate the SO($v'' = 0$) rise time to be longer than 100 ps by extrapolating the available data. At first glance, the prominent SO vibrational-level dependence seems to imply a nonstatistical behavior in which SO's of higher vibrational excitation are produced at higher rates. This can occur, for example, if the fast primary dissociation deposits a significant vibrational energy in the S−O stretch and rapid dissociation occurs before intramolecular vibrational energy redistribution (IVR) is completed. In such a case, SO fragments produced at earlier time should possess higher vibrational excitation, whereas those produced at a later time would contain lower vibrational energy because IVR should have drained energy from the SO moiety into other modes. However, the relatively long dissociation times (80−20 ps) observed here strongly suggest that the reaction takes place statistically after the IVR is completed, and such a nonstatistical behavior is unlikely to be dominant.

We believe that the product vibrational-level dependence observed here is simply a direct result of the broad internal energy distribution of CH_3SO above the C−S dissociation limit, as shown in Figure 17. Owing to the energy conservation constraint, higher vibrational levels of SO (and CH_3) products are accessible only by those CH_3SO's whose internal energies are high enough and thus appear at higher rates. Those CH_3SO's with lower internal energies simply cannot populate these higher product levels. On the other hand, lower vibrational levels of SO and CH_3, though they can originate from CH_3SO containing high internal energy, are probably mainly produced by those CH_3SO's containing energies that are only enough to populate the low vibrational level of SO. These CH_3SO's contain energies that are only slightly higher than the C−S bond energy and therefore dissociate very slowly. As a result, SO of low-v'' levels (0 and 1) appear more slowly than those of higher v'' (2 and 3)! We have shown above that a canonical averaging of RRKM rates over an estimated CH_3SO vibrational distribution gave an

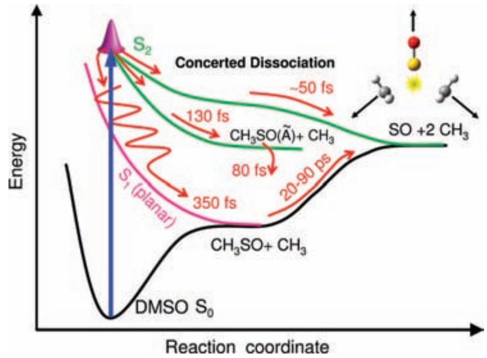

Figure 18. Schematic potential energy curves of states relevant to the photodissociation dynamics of DMSO at 200 nm and the proposed dissociation mechanism as discussed in the text. Curved arrows indicate the dissociation pathways.

average time constant of about 70 ps. As a comparison, an averaging over a CH_3SO subset with energy high enough to populate $SO(v'' = 6)$ yielded an average time constant of about 50 ps!

Because the slow SO and slow CH_3 components are the counter fragments of the same slow secondary decomposition, the partition of available energy into both fragments is expected to be statistical, and therefore, low-internal-energy CH_3 and SO are mostly formed in pair. Hence, the majority of vibrationless CH_3's are probably produced from the same subsets of CH_3SO that produce low-v'' SO and thus should rise on a similar time scale, that is, 80−100 ps. The dissimilarity between rise times of the slow CH_3 and slow SO of higher v'' arises simply because the latter are produced from CH_3SO subsets containing higher internal energies.

5. Conclusions

According to all experimental and theoretical results discussed above, we proposed a dissociation mechanism for the photodissociation of DMSO at 200 nm, as summarized schematically in Figure 18. Upon fs excitation of DMSO at 200 nm, a nuclear wave packet is launched on the S_2 surface. Dissociation and internal conversion then occur rapidly and competitively to move the system out of the probing window in about 30 fs. The majority of the trajectories on the S_2 surface go asymmetrically and result in breaking of a single C−S bond, whereas a small fraction of trajectories slide into the diagonal region and lead to a concerted, but not necessarily synchronous, breaking of the two C−S bonds. The single C−S bond breaking on the S_2 surface leads to electronically excited $CH_3SO(\tilde{A})$ and CH_3 products. The former rapidly internally converts to its ground state to produce internally hot $CH_3SO(\tilde{X})$. While the initial wave packet evolves adiabatically on the DMSO S_2 surface, a fraction of trajectories also undergo rapid internal conversion to the S_1 state. Once the system is in the S_1 surface, it starts executing large-amplitude inversion motions and slides down the S−C repulsive valley near a planar geometry. A fraction of the internally hot CH_3SO produced in the two primary dissociation pathways then undergoes slow secondary decomposition to produce SO and CH_3 on a time scale of few tens of picoseconds. Although it is difficult to determine the CH_3 quantum yield in the present study, this mechanism is qualitatively consistent with the reported quantum yield of ~1.1−1.5.[27−30] Note that the branching for the stepwise pathway is much greater than the concerted one, and hence, our conclusion is not inconsistent with most previous studies.[27−31]

An interesting result of this study is the observation of a concerted three-body dissociation pathway. Although an early study has inferred that the reaction proceeds through a concerted mechanism,[26] all subsequent works have concluded exclusively that the reaction follows a stepwise mechanism based on the observation of the reaction intermediate (CH_3SO).[27−31] Here, our results have shown that both types of reaction pathways can coexist and compete with each other adiabatically as well as nonadiabatically. This concept is indeed central to the reactivity and stereochemistry of a wide range of reactions, and we have demonstrated in our previous report[46] that the branching between the concerted and stepwise pathways can be controlled chemically.

In contrast to the conclusions of most previous reports,[27,30,31] the present study suggests that the S_0-dissociation pathway, even if it exists, does not play a significant role in the DMSO photochemistry at 200 nm excitation. The absence of S_0 dissociation in DMSO photolysis is probably well justified because internal conversion from S_2/S_1 to S_0 cannot compete with the much faster excited-state (S_2 and S_1) dissociation. Although DMSO $S_2 \rightarrow S_1$ internal conversion is expected to be extremely fast, $S_2 \rightarrow S_0$ and $S_1 \rightarrow S_0$ may not be very efficient because of much larger energy gaps involved. Acetone, which shares a similar size with DMSO, provides a good comparison.[23,24] Acetone $S_2 \rightarrow S_1$ internal conversion is relatively slow (~4 ps) due to a large S_2-S_1 energy gap (2.6 eV). The acetone S_1-state lifetime is strongly dependent on the internal energy. Near the zero point, the acetone S_1 lifetime is about 1.0 μs and is mainly due to internal conversion to S_0.[56] At higher energies, the acetone S_1-state relaxation is either due to intersystem crossing or, at higher energy, to α-C−C dissociation on the S_1 surface.[57] In all cases, $S_2/S_1 \rightarrow S_0$ internal conversions were found to be relatively slow processes and are not competitive with other more efficient decay channels. The scenario should be similar in DMSO as its S_2/S_1 dissociations are even much faster and should effectively suppress the formation of the hot DMSO ground state.

In conclusion, the present study has elucidated the dissociation dynamics of DMSO excited at 200 nm. The complexity of the reaction observed here is probably quite general for photodissociation of even relatively small molecules at a moderately high photon energy because many reaction pathways, including many-body dissociation, are energetically accessible. The simultaneous measurements of the temporal behaviors of all reaction products and the fs time-resolved KEDs proved to be crucial in unraveling such complex dissociation reactions.

Acknowledgment. This work was supported by the MOE Program for Promoting Academic Excellence of Universities (89-FA04-AA) and by the National Science Council of Taiwan, R. O. C.

References and Notes

(1) Maul, C.; Gericke, K. H. *Int. Rev. Phys. Chem.* **1997**, *16*, 1.

(2) Maul, C.; Gericke, K. H. *J. Phys. Chem. A* **2000**, *104*, 2531.

(3) North, S. W.; Longfellow, C. A.; Lee, Y. T. *J. Chem. Phys.* **1993**, *99*, 4423.

(4) Gejo, T.; Harrison, J. A.; Huber, J. R. *J. Phys. Chem.* **1996**, *100*, 13941.

(5) Ahmed, M.; Blunt, D.; Chen, D.; Suits, A. G. *J. Chem. Phys.* **1997**, *106*, 7617.

(6) Lee, Y. R.; Chou, C. C.; Lee, Y. J.; Wang, L. D.; Lin, S. M. *J. Chem. Phys.* **2001**, *115*, 3195.

(7) Lee, Y. R.; Chen, C. C.; Lin, S. M. *J. Chem. Phys.* **2004**, *120*, 1223.

(8) Scheld, H. A.; Furlan, A.; Huber, J. R. *J. Chem. Phys.* **1999**, *111*, 923.

(9) Continetti, R. E. *Annu. Rev. Phys. Chem.* **2001**, *52*, 165.

(10) Clements, T. G.; Luong, A. K.; Continetti, R. E. *Chem. Phys. Lett.* **2002**, *366*, 650.

(11) Zewail, A. H. *Angew. Chem., Int. Ed.* **2000**, *39*, 2587.

(12) Zewail, A. H. *J. Phys. Chem. A* **2000**, *104*, 5660.

(13) Trushin, S. A.; Fuss, W.; Kompa, K. L.; Schmid, W. E. *J. Phys. Chem. A* **2000**, *104*, 1997.

(14) Hertel, I. V.; Radloff, W. *Rep. Prog. Phys.* **2006**, *69*, 1897.

(15) North, S. W.; Blank, D. A.; Gezelter, J. D.; Longfellow, C. A.; Lee, Y. T. *J. Chem. Phys.* **1995**, *102*, 4447.

(16) Diau, E. W. G.; Abou-Zied, O. K.; Scala, A. A.; Zewail, A. H. *J. Am. Chem. Soc.* **1998**, *120*, 3245.

(17) Zhong, Q.; Poth, L.; Castleman, A. W. *J. Chem. Phys.* **1999**, *110*, 192.

(18) Diau, E. W. G.; Zewail, A. H. *ChemPhysChem* **2003**, *4*, 445.

(19) Kim, S. K.; Pedersen, S.; Zewail, A. H. *J. Chem. Phys.* **1995**, *103*, 477.

(20) Trentelman, K. A.; Kable, S. H.; Moss, D. B.; Houston, P. L. *J. Chem. Phys.* **1989**, *91*, 7498.

(21) Owrutsky, J. C.; Baronavski, A. P. *J. Chem. Phys.* **1999**, *110*, 11206.

(22) Diau, E. W. G.; Kotting, C.; Zewail, A. H. *ChemPhysChem* **2001**, *2*, 273.

(23) Chen, W. K.; Ho, J. W.; Cheng, P. Y. *J. Phys. Chem. A* **2005**, *109*, 6805.

(24) Chen, W. K.; Cheng, P. Y. *J. Phys. Chem. A* **2005**, *109*, 6818.

(25) Chen, W. K.; Ho, J. W.; Cheng, P. Y. *Chem. Phys. Lett.* **2005**, *416*, 291.

(26) Chen, X. R.; Wang, H. X.; Weiner, B. R.; Hawley, M.; Nelson, H. H. *J. Phys. Chem.* **1993**, *97*, 12269.

(27) Blank, D. A.; North, S. W.; Stranges, D.; Suits, A. G.; Lee, Y. T. *J. Chem. Phys.* **1997**, *106*, 539.

(28) Rudolph, R. N.; North, S. W.; Hall, G. E.; Sears, T. J. *J. Chem. Phys.* **1997**, *106*, 1346.

(29) Zhao, H. Q.; Cheung, Y. S.; Heck, D. P.; Ng, C. Y.; Tetzlaff, T.; Jenks, W. S. *J. Chem. Phys.* **1997**, *106*, 86.

(30) Thorson, G. M.; Cheatum, C. M.; Coffey, M. J.; Crim, F. F. *J. Chem. Phys.* **1999**, *110*, 10843.

(31) Pino, G. A.; Torres, I.; Amaral, G. A.; Aoiz, F. J.; Banares, L. *J. Phys. Chem. A* **2004**, *108*, 8048.

(32) Amaral, G. A.; Torres, I.; Pino, G. A.; Aoiz, F. J.; Banares, L. *Chem. Phys. Lett.* **2004**, *386*, 419.

(33) Drage, E. A.; Cahillane, P.; Hoffmann, S. V.; Mason, N. J.; Limao-Vieira, P. *Chem. Phys.* **2007**, *331*, 447.

(34) Bond enthalpies are calculated using experimental heats of formation at 0 K for DMSO, CH_3, and SO from ref 35 and a theoretical (G2(MP2)) heat of formation at 0 K for CH_3SO from ref 29.

(35) Lias, S. G.; Bartmess, J. E.; Liebman, J. F.; Holmes, J. L.; Levin, R. D.; Mallard, W. G. *J. Phys. Chem. Ref. Data* **1988**, *17*, 1.

(36) Mordaunt, D. H.; Osborn, D. L.; Neumark, D. M. *J. Chem. Phys.* **1998**, *108*, 2448.

(37) Cheng, P. Y.; Zhong, D.; Zewail, A. H. *J. Chem. Phys.* **1996**, *105*, 6216.

(38) Hudgens, J. W.; Digiuseppe, T. G.; Lin, M. C. *J. Chem. Phys.* **1983**, *79*, 571.

(39) Clerbaux, C.; Colin, R. *J. Mol. Spectrosc.* **1994**, *165*, 334.

(40) Yamasaki, K.; Taketani, F.; Tomita, S.; Sugiura, K.; Tokue, I. *J. Phys. Chem. A* **2003**, *107*, 2442.

(41) Yamasaki, K.; Taketani, F.; Sugiura, K.; Tokue, I.; Tsuchiya, K. *J. Phys. Chem. A* **2004**, *108*, 2382.

(42) The kinetic model used to fit the early time transient includes a DI component, which is simply the 350 nm off-resonance transient with an adjustable amplitude, and two neutral CH_3 components derived from the proposed mechanism described in section 4.

(43) Zare, R. N. *Mol. Photochem.* **1972**, *4*, 1.

(44) Dantus, M.; Rosker, M. J.; Zewail, A. H. *J. Chem. Phys.* **1988**, *89*, 6128.

(45) Rose, T. S.; Rosker, M. J.; Zewail, A. H. *J. Chem. Phys.* **1989**, *91*, 7415.

(46) Ho, J. W.; Chen, W. K.; Cheng, P. Y. *J. Am. Chem. Soc.* **2007**, *129*, 3784.

(47) Frisch, M. J. Trucks, G. W.; Schlegel, H. B.; Scuseria, G. E.; Robb, M. A.; Cheeseman, J. R.; Montgomery, J. A., Jr.;Vreven, T.; Kudin, K. N.; Burant, J. C.; Millam, J. M.; Iyengar, S. S.; Tomasi, J.; Barone, V.; Mennucci, B.; Cossi, M.; Scalmani, G.; Rega, N.; Petersson, G. A.; Nakatsuji, H.; Hada, M.; Ehara, M.; Toyota, K.; Fukuda, R.; Hasegawa, J.; Ishida, M.; Nakajima, T.; Honda, Y.; Kitao, O.; Nakai, H.; Klene, M.; Li, X.; Knox, J. E.; Hratchian, H. P.; Cross, J. B.; Bakken, V.; Adamo, C.; Jaramillo, J.; Gomperts, R.; Stratmann, R. E.; Yazyev, O.; Austin, A. J.; Cammi, R.; Pomelli, C.; Ochterski, J. W.; Ayala, P. Y.; Morokuma, K.; Voth, G. A.; Salvador, P.; Dannenberg, J. J.; Zakrzewski, V. G.; Dapprich, S.; Daniels, A. D.; Strain, M. C.; Farkas, O.; Malick, D. K.; Rabuck, A. D.; Raghavachari, K.; Foresman, J. B.; Ortiz, J. V.; Cui, Q.; Baboul, A. G.; Clifford, S.; Cioslowski, J.; Stefanov, B. B.; Liu, G.; Liashenko, A.; Piskorz, P.; Komaromi, I.; Martin, R. L.; Fox, D. J.; Keith, T.; Al-Laham, M. A.; Peng, C. Y.; Nanayakkara, A.; Challacombe, M.; Gill, P. M. W.; Johnson, B.; Chen, W.; Wong, M. W.; Gonzalez, C.; Pople, J. A. Gaussian 03, revision B.01; Gaussian, Inc.: Pittsburgh, PA, 2003.

(48) Mondejar, V. P.; Yusa, M. J.; Cuesta, I. G.; de Meras, A. M. J. S.; Sanchez-Marin, J. *Theor. Chem. Acc.* **2007**, *118*, 527.

(49) Cubbage, J. W.; Jenks, W. S. *J. Phys. Chem. A* **2001**, *105*, 10588.

(50) Green, W. H.; Moore, C. B.; Polik, W. F. *Annu. Rev. Phys. Chem.* **1992**, *43*, 591.

(51) The maximum CH_3 COM speed observed in this work is 4400 m/s, corresponding to a relative recoil speed of about 5500 m/s for the CH_3 and CH_3SO pair.

(52) Busch, G. E.; Wilson, K. R. *J. Chem. Phys.* **1972**, *56*, 3638.

(53) In the SO transient, the concerted dissociation component accounts for about 10−15% of the total signal. Each SO radical is produced along with two CH_3 radicals in the concerted pathway. Assuming that the overall CH_3 quantum yield is 1.5, each SO radical produced in the stepwise pathway must be accompanied by three CH_3 radicals. Therefore, CH_3 produced in the concerted channel can be estimated to be about 7−10% of total CH_3 signal.

(54) The average rate is calculated using $\langle k \rangle = \int_{E_0}^{E_{av}} k(E)P(E)\mathrm{d}E / \int_{E_0}^{E_{av}} P(E)\mathrm{d}E$, where $k(E)$ is the energy-dependent RRKM rate, E_{av} is the available energy, E_0 is the dissociation limit, and $P(E)$ is the vibrational energy distribution of the hot CH_3SO ensemble.

(55) Yamasaki, K.; Tomita, S.; Hatano, T.; Taketani, F.; Tokue, I. *Chem. Phys. Lett.* **2005**, *413*, 231.

(56) Anner, O.; Zuckermann, H.; Haas, Y. *J. Phys. Chem.* **1985**, *89*, 1336.

(57) Blitz, M. A.; Heard, D. E.; Pilling, M. J. *J. Phys. Chem. A* **2006**, *110*, 6742.

JP804847Y